NTNU – Trondheim
Norwegian University of
Science and Technology

Numerical Investigations on Nanobubble Stability

Knut Sverdrup Kleppestø

Master of Science in Physics and Mathematics
Submission date: June 2015
Supervisor: Peter Berg, IFY

Norwegian University of Science and Technology
Department of Physics

Abstract

This thesis discusses the stability and lifetime of bulk and surface nanobubbles. Two numerical models are presented which have been developed in order to investigate aspects of the dynamic equilibrium mechanism using computational methods. By using a steady-state approach where a surface nanobubble is sustained by electrolysis, it is found that for a given nanobubble size and geometry there is only a very narrow range of possible molar fluxes into the system which balance it. This demonstrates the importance of the dynamic equilibrium mechanism in sustaining the surface nanobubbles. An effort to find a better approximation of the expected lifetimes of bulk nanobubbles has also proven fruitful. Preliminary results show lifetimes that are an order of magnitude longer than those previously presented in the literature.

Sammendrag

I denne masteroppgaven drøftes stabiliteten og levetiden til nanobobler som er fullstendig omsluttet av vann eller som befinner seg på en overflate. To numeriske modeller har blitt utviklet for å undersøke aspekter ved dynamisk-likevekt-mekanismen. Ved å bruke en tilnærming hvor en overflatenanoboble opprettholdes i en uforanderlig tilstand gjennom elektrolyse har vi funnet at det kun finnes noen få verdier for molar strømning inn i systemet som gir riktig balanse for en gitt størrelse og geometri på boblen. En innsats for å finne en bedre tilnærming for levetiden til frie nanobobler i væske har også vært fruktbar. Foreløpige resultater viser levetider som er en størrelsesorden lengre enn dem presentert ellers i litteraturen.

Acknowledgements

Gratitude should be directed towards:

- Peter Berg
- Sven-Joachim Kimmerle
- Elg, Mats, Lazerblade
- Mom and dad
- Ingunn

Contents

List of Figures

List of Tables

Nomenclature

Physical constants

Symbol	Description	Value	Units
$A_{\mathrm{H_2}}$	Collisional cross section for $\mathrm{H_2}$	$1.412 \cdot 10^{-19}$	$\mathrm{m^2}$
H	Dimensionless Henry's constant for $\mathrm{H_2}$	$1.907 \cdot 10^{-2}$	–
k_B	Boltzmann's constant	$1.3807 \cdot 10^{-23}$	J/K
p_0	Atmospheric pressure	101,325	Pa
R	Gas constant	8.31446	J/(K mol)
γ	Surface tension of water at 25°C	$7.280 \cdot 10^{-2}$	N/m

Variables and parameters

Symbol	Description	Units
A_S	Area of nanobubble surface S	$\mathrm{m^2}$
C_g	Hydrogen concentration in gas phase	$\mathrm{mol/m^3}$
C_l	Hydrogen concentration in liquid phase	$\mathrm{mol/m^3}$
D_l	Diffusion constant for $\mathrm{H_2}$ in liquid phase	$\mathrm{m^2/s}$
h_b	Nanobubble height	m
J	Molar flux of hydrogen	$\mathrm{mol/(m^2\,s)}$
Kn	Knudsen number	–
p_g	Pressure of gas inside the nanobubble	Pa
r_b	Lateral nanobubble radius	m
$\mathcal{R}$	Nanobubble radius of curvature	m
t_l	Dissolution time for bulk nanobubble	s

T	System temperature	K
v_l	Liquid velocity	m/s
α	Mass transfer coefficient for gas/liquid interface	m/s
η	Nanobubble radius relative to initial size	–
θ	Gas-side contact angle between nanobubble surface and solid	°
λ	Molecular mean-free path	m
μ	Chemical potential of hydrogen	J/mol
σ	Local entropy production	$\mathrm{J/(K\,m^3\,s)}$

Chapter 1

Introduction

Nanobubbles are gaseous domains on the nanoscale that have received widespread attention over the last decade. This is partly due to the increasing amount of areas in industry to which they can be applied, but also due to the fact that basic properties observed experimentally, are yet to be explained theoretically in a satisfactory manner. In particular, the low contact angles for surface nanobubbles compared to macroscopic ones and their extremely high stabilities, and thus lifetimes, have puzzled the scientific community, and remain open questions. Among several proposed models to explain these properties, one which has received much acclaim is the dynamic-equilibrium model. It suggests that the high Laplace pressure calculated classically is tolerated due to a stable balance of gas in- and out-flux through the bubble surface.

Apart from simulations in molecular dynamics, there have been no thorough numerical investigations of this model to the best of the author's knowledge, and as such two numerical schemes have been developed to study different aspects of nanobubble stability. In order to investigate the validity of the dynamic equilibrium model and to describe the relationship between flow through the bubble surface and gas production in the liquid, a finite-element scheme has been implemented in MATLAB to simulate a single surface nanobubble in stable dynamic equilibrium in both two (2D) and three (3D) dimensions. The work is a continuation of the research carried out as a part of a specialization project by the author[1] and is closely connected with Sperre's master's thesis[2]. The second model we have developed simulates the dissolution of a bulk nanobubble to find a better estimation for their expected lifetimes. A finite-difference scheme on a shrinking, time-dependent ”rubber band” domain has been written in C++ to compute the behaviour of this system.

Since much of the work presented in the aforementioned specialization-project report[1] is important for what we present in this thesis, it has been included. For clarification, it should be stressed that sections 2.1-2.2 are only slightly altered and expanded versions of that report, and that the explanation of the finite-element method in section 2.4.1

and appendix C have merely been expanded to include the treatment of Robin boundary conditions. The numerical model of section 3.1 is based on a simpler model (with a flat-bubble approximation) developed in the project.

Chapter 2 includes a review of the current progress in the field of nanobubbles and their stability, in addition to some theory on the thermodynamics of the system, existing solutions for calculating lifetimes of bulk bubbles, and a brief overview of the numerical methods employed. In chapter 3, both of the numerical models are explained. We go through the modelling of the system under consideration, along with the numerical methods for discretization and computational algorithms. The results of the numerical simulations are given in chapter 4, with a discussion of these following in chapter 5. Some suggestions regarding what the continuation of this work could encompass, are given in chapter 6. Chapter 7 concludes the thesis.

Chapter 2

Experimental evidence and theoretical background

2.1 Nanobubbles

2.1.1 Current research

Nanobubble is a term used to describe gaseous domains with spatial extent on the nanometre scale. They can occur in liquids (as bulk nanobubbles) and on boundaries between liquids and solids (as either surface nanobubbles or so-called micropancakes). In this thesis we will be considering both steady-state surface nanobubbles and dissolving bulk nanobubbles, but the two types are referred to commonly as nanobubbles. Micropancakes are outside the scope of this thesis.

The existence of nanobubbles was suggested to explain long-range hydrophobic attraction as early as 1994[3], but they were not observed experimentally until tapping-mode atomic force microscopy (TMAFM) was applied to investigate gas phases in 2000[4,5]. Figure 2.1 shows how the controlled growth of nanobubbles can be visualized using this technique. In recent years, this phenomenon has received a lot of attention in various research fields because of its peculiar properties and behaviour, and especially because of a lack of satisfactory explanations and physical theories. In particular, an explanation for the extremely high stability of surface nanobubbles is sought.

Nanobubbles have been electrolytically generated in large numbers on highly oriented pyrolytic graphite (HOPG) surfaces[4,6,7], silicon wafers[5] and other materials, and recently individual surface nanobubbles with radii of less than 50 nm have even been generated on Platinum nanodiscs[8]. This last achievement lays the foundation for one of the numerical schemes developed in this thesis. Their geometric properties have been studied extensively through the use of TMAFM[4–7,9,10], quartz crystal microbalance[11,12], surface plasmon resonance[13] and rapid cryo-fixation[14], yielding correlating results. Since so many different tools have been used to investigate nanobubbles, there is now little

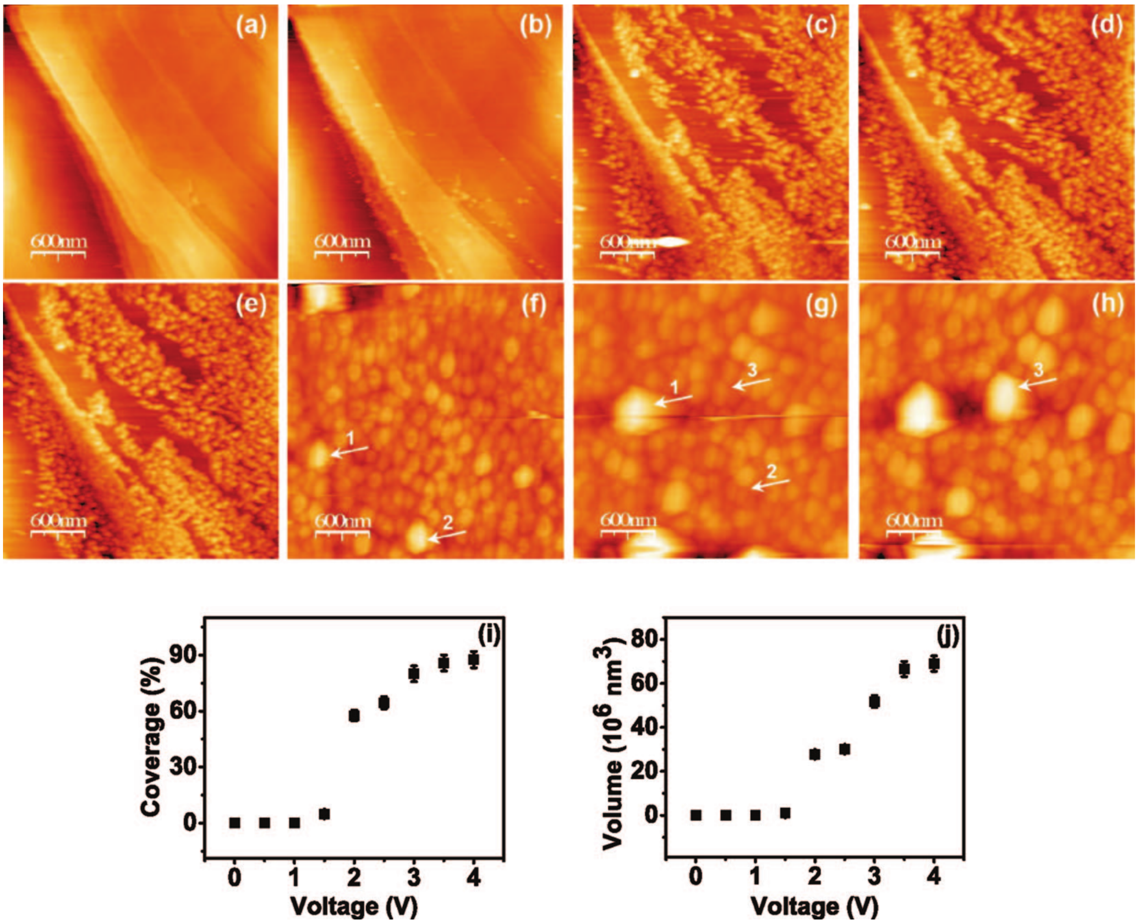

Figure 2.1: TMAFM topography images show nanobubble formation for different voltages and height ranges (a)-(f). The plots in (i) and (j) show the dependencies of the nanobubble coverage and volume on the applied voltage. Image printed with permission from Yang et al.[6]

doubt that they are indeed gaseous domains, and that they occur naturally. An example of an investigation of the geometrical properties of nanobubbles is shown in figure 2.2.

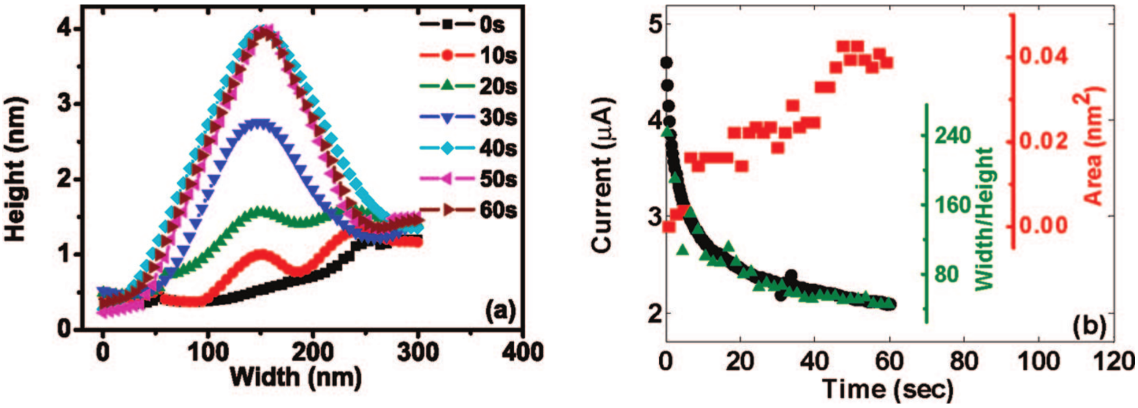

Figure 2.2: Geometrical properties of nanobubbles and how they develop, with results from TMAFM. The left plot shows the height above the surface on an area where a single surface nanobubble has formed at different times, while the right plot shows how the current drops as the bubbles begin to form and decrease the rate of electrolysis. Image printed with permission from Yang et al.[6]

Recent progress has also been made in the study of nanobubble nucleation by combining analytical techniques from statistical physics with TMAFM images[15]. As shown in figure 2.3, image recognition can be used to analyse the placement and relative sizes of nanobubbles in clusters by drawing Voronoi and Appolonius (modified Voronoi) diagrams. The information read out from these diagrams can then be used to theorize what factors have a direct effect on nanobubble nucleation.

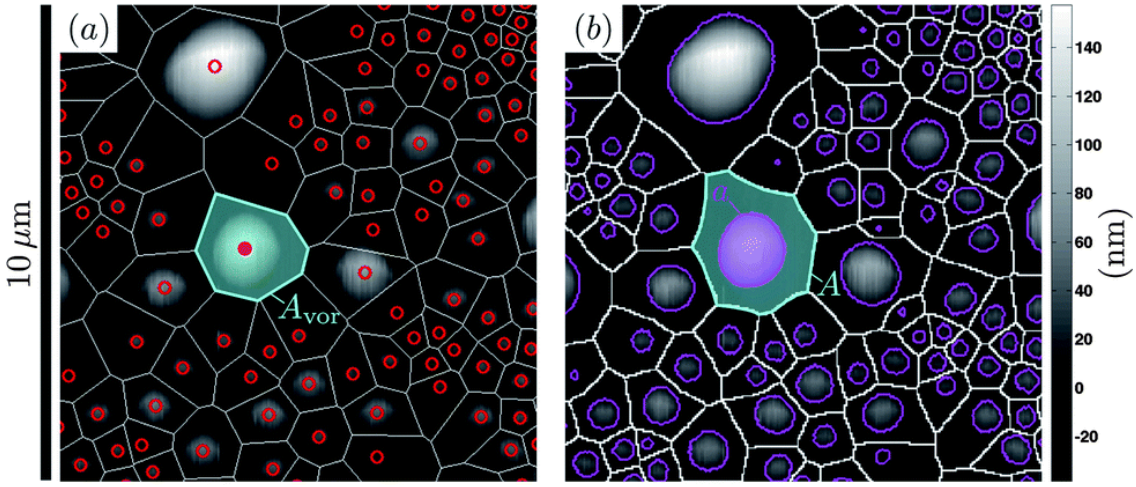

Figure 2.3: TMAFM images with superimposed geometric structures. Voronoi diagrams shown in (a) have cells defined such that each point in a cell is closer to that cell's nanobubble center than any other, while the boundaries in modified Voronoi diagrams like those in (b) are closer to that cell's nanobubble border than any others. Image printed with permission from Lhuissier et al. [15]

2.1.2 Surface nanobubbles

In our consideration of surface nanobubbles that form on the solid/liquid interface, we will always study nanobubbles that already exist, and as such we do not concern ourselves with bubble nucleation. We also assume that they take the form of spherical caps, within which the gas exists. The geometry is shown in figure 2.4, where the radius of curvature $\mathcal{R}$, lateral bubble radius r_b, bubble height h_b and contact angle θ are introduced. From figure 2.4, the measurable quantities can be written as functions of $\mathcal{R}$ and θ.

$$r_b = \mathcal{R}\cos\left(\frac{\pi}{2} - \theta\right) = \mathcal{R}\sin\theta \tag{2.1}$$

$$h_b = \mathcal{R}\left(1 - \sin\left(\frac{\pi}{2} - \theta\right)\right) = \mathcal{R}(1 - \cos\theta) \tag{2.2}$$

We can also express the radius of curvature as a function of the bubble's height and radius,

$$\mathcal{R} = \frac{r_b^2 + h_b^2}{2h_b}\,. \tag{2.3}$$

Experimental results show that surface nanobubbles can have widths $2r_b$ in the range

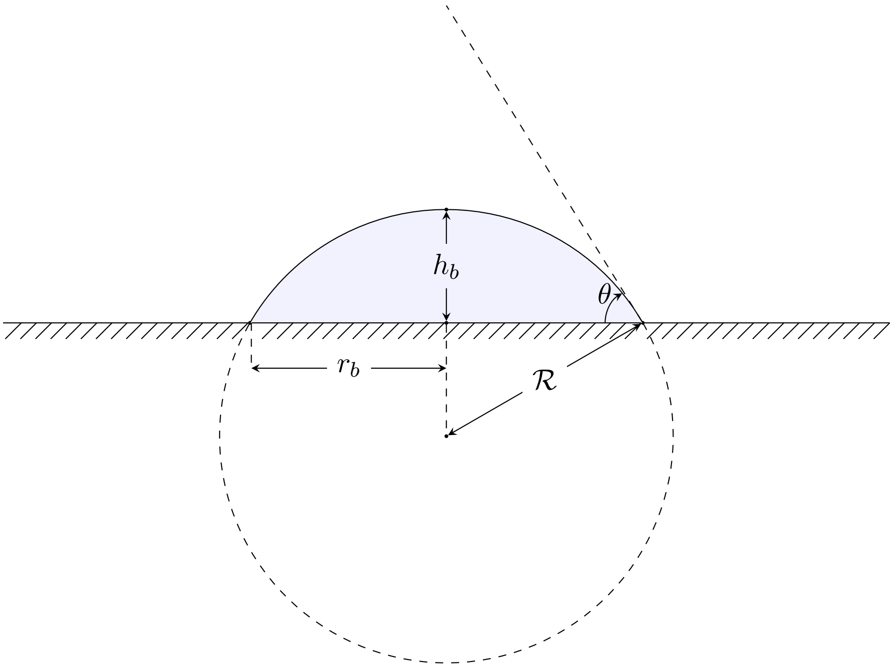

Figure 2.4: Geometry of a surface nanobubble. The bubble is a spherical cap with radius of curvature $\mathcal{R}$ and gas-side contact angle θ. The disc on the solid covered by the bubble has radius r_b, while the bubble's maximum height over the interface is h_b. Note that the contact angle has been enlarged significantly to show the relationship between the different lengths.

50 nm - 500 nm, and heights h_b of approximately a tenth of r_b, all depending on how the bubbles are generated and what type of materials are used. Inserting these numbers into (2.3) yields typical radii of curvature of 100 nm - 1000 nm and contact angles around 15°. These low contact angles turn out to be characteristic for surface nanobubbles. In fact, all observed surface nanobubbles have gas-side contact angles of 10°-30°, regardless of whether the solid surface is hydrophobic or hydrophilic[16]. The contact angle seems to depend strongly on the gas type in the bubble, which is in contrast to macroscopic bubbles, where the solid and liquid are the only materials that the contact angle depends strongly on. In addition to this, the contact angle of a surface nanobubble varies with the radius of the bubble. A proposed relationship between the contact angle θ and lateral bubble radius r_b is[17]

$$\cos\theta = \cos\theta_\infty - \frac{\cos\theta_\infty - \cos\theta_0}{1 + r_b/\delta} . \tag{2.4}$$

Here, θ_∞ and θ_0 are the limiting cases of the contact angle when r_b approaches infinity and zero, respectively, while δ is a length constant for a nanoscopic correction of the macroscopic contact angle. Figure 2.5 shows a plot of (2.4) with $\theta_0 = 0$, which is a standard choice for this angle since it works well for very small bubbles. It is evident that the contact angle approaches the macroscopic contact angle θ_∞ for large radii, but has a strong dependency on r_b in the small-bubble limit. This dependency of the contact angle on the bubble radius, which is unique for surface nanobubbles, seems to be an important

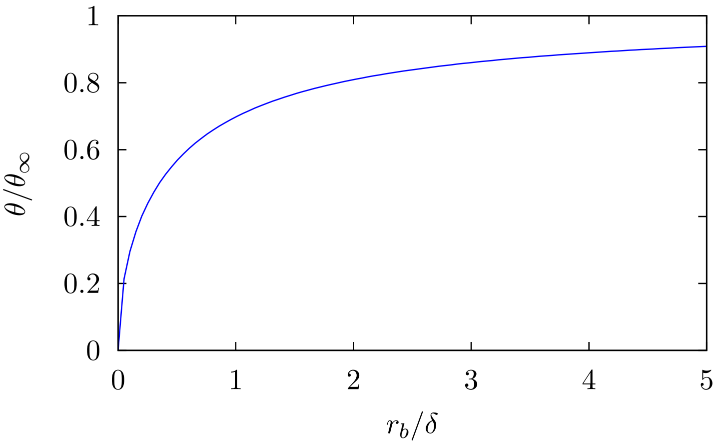

Figure 2.5: Contact angle θ as a function of bubble radius r_b.

factor in explaining the remarkable stability of nanobubbles. The dependency itself must of course be explained, along with a more encompassing explanation for the superstability, and as such several theories and models have been proposed.

2.1.3 Stability of surface nanobubbles

As mentioned previously, we do not concern ourselves with the formation of nanobubbles. It should be noted, however, that nanobubble nucleation occurs under special circumstances, such as strong electrolysis, ultrasonication or through the solvent exchange procedure. When the stability of surface nanobubbles are discussed in this thesis, we are considering systems at a state after the formation is complete.

According to most papers on nanobubbles, the experimentally observed lifetimes of surface nanobubbles exceed their expected values from classical thermodynamics by many orders of magnitude[18]. In other words, they are surprisingly stable. A thermodynamic viewpoint suggests a lifetime based on the (Laplace) pressure difference between the interior and exterior of the bubble (2.21), which is described in detail in subsection 2.2.2. With the very small radii of curvature observed in nanobubbles, the Laplace pressure is very high, thereby driving bubble dissolution, and thus equilibrium should not be sustained. The question of why nanobubbles are so stable is still open, and much research has been done to figure it out. Several theories have been put forward to explain the stability, most notably the effects of impurities in the system[19,20], the dynamic-equilibrium model[17,21] and the combined effect of clustering, limited diffusion through the far field and pinned contact lines[22].

Impurities in surface layer and liquid/gas interface

This model, first presented by Ducker[19], considers the effect of impure anomalies both in the solid surface layer and in the interface between the bubble and the liquid. A thin film of contaminants can reduce both the contact angle and the Laplace pressure because of its lowering of the surface tension. A faster increase in surface tension than the corresponding decrease in the area of the gas-liquid interface will lead to a stabilization of bubbles. A thorough deliberation on this theory was made by Das[20], who included detailed calculations on the role of both ionic and nonionic impurities on the solid surface. This showed that even a small bulk concentration of impurities can reduce the contact angle to observed values. It does not, however, give a low enough Laplace pressure of the bubbles to explain the long lifetime. As such it gives evidence that the role of impurities does indeed lower the nanobubble contact angle, but this theory is widely considered to be incomplete due to its failure to explain nanobubble stability.

Dynamic-equilibrium model

An explanation for the high stability that has received more acceptance than the impurity model is the dynamic-equilibrium model[17,21]. It is the purpose of this study to simulate this model numerically. In the dynamic-equilibrium model, the flux of hydrogen through the bubble/liquid interface is balanced exactly in order to achieve equilibrium. We thus do not have chemical equilibrium in the classical sense, since there is a constant movement of components into and out of the bubble. The stability of the nanobubbles is therefore described by a dynamic equilibrium, hence the name of the model. To achieve a dynamic equilibrium, there must also be a circulation of hydrogen in the exterior of the bubble, so that hydrogen is constantly available at the liquid/solid interface near the edge of the bubble. Figure 2.6 shows the flow schematically. Mathematically, we have dynamical equilibrium if

$$\int_S \mathbf{J} \cdot \hat{\mathbf{n}} \, \mathrm{d}S = 0 \,. \tag{2.5}$$

Here, $\mathbf{J}$ is the diffusive flux vector for hydrogen and $\hat{\mathbf{n}}$ is the outward unit normal vector on the bubble surface S over which the surface integral is evaluated.

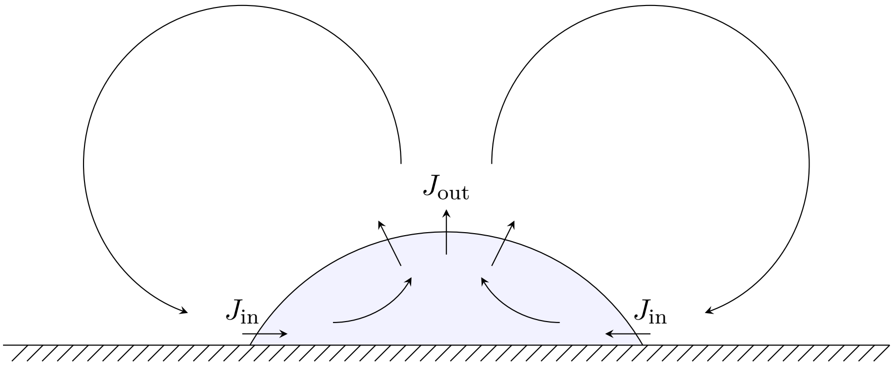

Figure 2.6: Dynamic-equilibrium model for the explanation of surface nanobubble stability. The arrows indicate the flow of hydrogen in an around the nanobubble. The total fluxes into and out of the bubble/liquid interface are denoted J_{in} and J_{out}, respectively.

In the system which we are considering, the generation of nanobubbles is done through electrolysis, which is the process of combining aqueous hydrogen ions (H^+) with electrons (e^-) brought through a solid to the solid/liquid interface. The reaction yields hydrogen gas through the balanced chemical equation

$$2H^+(aq) + 2e^- \rightleftharpoons H_2(g)\,. \tag{2.6}$$

Electrolysis can occur anywhere on a catalyst surface where an electrical current provides electrons. Since a nanobubble covers a disc of radius r_b on the interface, this area is inaccessible to electrolysis after the bubble has formed. The hydrogen gas being produced in the vicinity of the bubble becomes the main source of influx for sustaining a dynamic equilibrium. Figure 2.7 displays electrolysis near the nanobubble. That nanobubble nucleation leads to a drop in current has been verified experimentally with single nanobubbles formed on platinum nanodiscs with radii smaller than 25 nm[8].

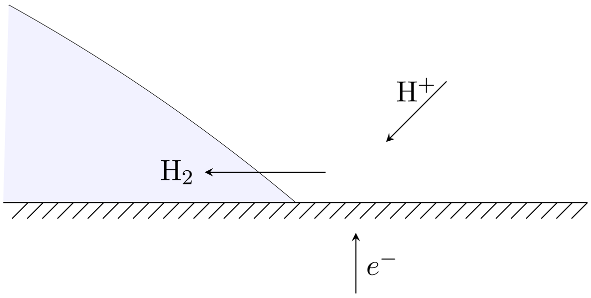

Figure 2.7: Electrolysis near the nanobubble surface.

Knudsen gas behaviour

Since the dynamic-equilibrium model depends on a local circulation of hydrogen gas near the nanobubble, there must be some driving mechanism that supplies the energy required to do so. It turns out that if the gas in the nanobubble is of Knudsen type, the geometry of the system allows the solid substrate to be treated as a heat bath which provides this energy thermally[10]. It is not evident that treating the substrate as a heat bath (i.e. giving gas molecules higher energy after collision with it than before) makes sense when the temperature is constant in the system, but the energy amounts are so small that studying energy conservation becomes difficult due to thermal leakage. Nevertheless, let us assume for a moment that the thermal drive stems from the substrate. The condition for a gas to be of Knudsen type is that its Knudsen number Kn, given by the ratio of the mean free path λ of the molecule to the container length scale, in our case h_b, is greater than unity[23], i.e.

$$\mathrm{Kn} = \frac{\lambda}{h_b} > 1\,. \tag{2.7}$$

For an ideal gas, the mean free path is given by

$$\lambda = \frac{k_B T}{\sqrt{2} A_{\mathrm{H}_2} p_g}\,, \tag{2.8}$$

where $k_B = 1.3807 \cdot 10^{-23}\,\mathrm{J/K}$ is Boltzmann's constant, $A_{\mathrm{H}_2} = 1.412 \cdot 10^{-19}\,\mathrm{m}^2$ is the collisional cross section for hydrogen gas and p_g is the pressure of the gas inside the nanobubble. For a typical nanobubble of radius 50 nm and contact angle 15°, and calculating p_g from (2.22) derived in subsection 2.2.2, the Knudsen number is 3.7, so Knudsen behaviour is indeed observed. This is true for the geometries of all observed nanobubbles in the literature[10], and might explain the origins of the driving force for the circulation of H_2 near the nanobubble, which is a crucial element in the validity of the dynamic-equilibrium model. In the system with electrolysis which we are considering, however, this problem is removed by the constant production of hydrogen gas through electrolysis.

Clustering, limited diffusion through far field and contact line pinning

According to Weijs et al.[22], the longevity of surface nanobubbles is due to a combination of three factors, namely the tendency of surface nanobubbles to form in clusters with many nanobubbles, the fact that diffusion of gas through liquid is limited by the far field boundary condition, and the angular contact line pinning of nanobubbles. In their paper, it is argumented that the relevant length scale for the system is the distance from the surface nanobubble to the liquid/air interface, and not the bubble radius of curvature, which yields the appropriate time scale for dissolution. The model gives both numerical and analytical results to support experimental data, and is explained well. The main problem with this model is the assumption that Henry's law holds on the bubble surface, i.e. that we have chemical equilibrium across the boundary. This may, however, not play a significant role. Regardless, the model is perhaps the most complete explanation for the stability of surface nanobubbles to date. Unfortunately, the author of this thesis discovered this interesting paper only at the end of his MSc research, preventing comparisons with our findings.

2.1.4 Applications

There are a multitude of possible applications of nanobubbles, both in systems where they are desirable and ones where they are not. The number of areas where nanobubbles are being applied and possibly can be applied in a constructive manner in the future is extensive, and an excellent overview is found in the paper by Seddon et al. from 2012[16].

An example of an area where nanobubbles are undesirable is in hydrogen production through proton exchange membrane (PEM) water electrolysis. This is the most reliable method for producing pure hydrogen, which acts as an efficient energy carrier for PEM fuel cells. Such fuel cells have great promise as renewable energy sources with no harmful emissions, but are only slowly becoming a viable technology, partly due to their low efficiency and partly due to the high cost of hydrogen production. A more robust understanding of nanobubbles can possibly help create more efficient and economical environments for electrolysis without this weakness.

Since surface nanobubbles have the ability to remove adsorbed proteins from substrates[24–27], they can be used as nanoscopic cleaning agents with no risk of damaging surfaces or being chemically hazardous[12,28]. This is particularly relevant in the semiconductor industry.

There is also good reason to believe that nanobubbles can be applied for slip-control in microfluidics[29,30]. Since the flow rate in such devices is governed by the no-slip boundary condition, walls that are not wetted because of a layer of nanoscopic gas bubbles will have a local breakdown for this condition and allow flow with reduced resistance. In such a manner, electro-osmotic flows can possibly be greatly amplified in microfluidic devices[31].

2.2 Thermodynamics

2.2.1 Convection, advection and diffusion

To be able to analyse a nanobubble system in light of the dynamic-equilibrium model, the most important condition to investigate is that of net hydrogen flux through the nanobubble surface. Since the transport of hydrogen in the system is of such importance, we need to discuss the equations which govern the hydrogen concentration as a function of time and space. We therefore introduce the terms convection, advection and diffusion. Convection is the concerted, collective movement of a group of molecules within a fluid, either through advection or diffusion, and as such is a collective term for these two. Advection denotes the transport due to overall movement of the fluid, while diffusion is caused by the intermingling of substances due to the natural movement of the particles. To get an intuitive understanding of the difference, we can think of advection as mass transport due to the liquid velocity, while diffusion is caused by concentration differences throughout the liquid. Convection describes the total molecular transport in the liquid. In the literature these terms are used somewhat ambiguously, and it is especially common to see convection described as advection and vice versa.

Scalar transport equation

The generic scalar transport equation, also known as the convection-diffusion or advection-diffusion equation (and which could, arguably, be known as just the convection equation), is a partial differential equation which describes the convection of a species in a system through advection and diffusion. To derive it, we consider conservation of hydrogen gas in a liquid. This is described by the continuity equation

$$\dot{C}_l + \nabla \cdot \mathbf{J} = \Xi \,, \tag{2.9}$$

where C_l is the concentration of hydrogen dissolved in the liquid, $\mathbf{J}$ is the molar flux of hydrogen and Ξ denotes any sources or sinks for hydrogen, for example due to chemical reactions. In this thesis, we do not consider any such sources or sinks, and therefore set $\Xi = 0$. This assumption will be discussed in more detail shortly. In words, the continuity equation states that the rate of change of hydrogen concentration with respect to time plus the divergence of the flux in a given test volume equals the sum of sources and sinks within that volume. As described earlier, the convective molar flux is due partly to advection and partly due to diffusion. We therefore set

$$\mathbf{J} = \mathbf{J}_{\text{advection}} + \mathbf{J}_{\text{diffusion}} \,. \tag{2.10}$$

The advective term is merely the transport of hydrogen due to the liquid velocity $\mathbf{v}_l$, and as such given by

$$\mathbf{J}_{\text{advection}} = \mathbf{v}_l C_l \,.$$

In order to describe the diffusive flux we employ Fick's first law, which states that the flux is proportional to the concentration gradient in the liquid, i.e.

$$\mathbf{J}_{\text{diffusion}} = -D_l \nabla C_l \,,$$

where the proportionality factor D_l is the diffusion coefficient of hydrogen gas in the liquid (in our case water). A more thorough derivation of Fick's first law will be presented from non-equilibrium thermodynamics shortly. Combining these two in (2.10) and inserting it in (2.9), remembering also that the sources and sinks have been neglected, we have

$$\dot{C}_l = D_l \Delta C_l - \nabla \cdot (\mathbf{v}_l C_l) \,, \tag{2.11}$$

which is the generic scalar transport equation without source and sink terms. We will employ (2.11) to calculate the lifetime of a bulk hydrogen nanobubble in water.

Steady-state case

If we consider a steady-state system, i.e. one where the concentration is time-independent, and assume convection to be solely driven by diffusion, (2.11) takes the form of the Laplace equation,

$$\Delta C_l = 0 \,. \tag{2.12}$$

In order to validate the dynamic equilibrium mechanism for a surface nanobubble stabilized by electrolysis at a platinum electrode, we will be considering this simpler governing equation.

Non-equilibrium thermodynamics

For a better understanding of the assumptions made in the preceding subsection, we turn to the field of non-equilibrium thermodynamics. The theory of non-equilibrium thermodynamics, as given here, is inspired by Kjelstrup et al.[32], which is a unique resource for understanding this highly relevant field. As stated earlier, "dynamic equilibrium" merely implies that the concentration throughout the system is time-independent, even though there is a constant diffusive flux which stabilizes the bubble. In non-equilibrium thermodynamics, systems are characterized by their local entropy production σ, which in general is given by a sum of n conjugate flux and force pairs as

$$\sigma = \sum_{i=1}^{n} \mathbf{X}_i \cdot \mathbf{J}_i \,, \tag{2.13}$$

where $\mathbf{X}_i$ denotes forces and $\mathbf{J}_i$ fluxes. The different fluxes can be written in terms of the forces by introducing the Onsager coefficients L_{ij},

$$\mathbf{J}_i = \sum_{j=1}^{n} L_{ij} \mathbf{X}_j \,. \tag{2.14}$$

Thermodynamic systems have entropy productions given by

$$\sigma = -\frac{1}{T^2}\,\mathbf{J}'_q \cdot \nabla T - \frac{1}{T}\sum_{i=1}^{n} \mathbf{J}_i \cdot \nabla \mu_{i,T} - \frac{1}{T}\,\mathbf{j} \cdot \nabla \phi - r\frac{\Delta_r G}{T} \,. \tag{2.15}$$

Here, $\mathbf{J}'_q$ is the heat flux, T is the temperature, $\mathbf{J}_i$ is the diffusive flux of component i, μ_i is the chemical potential of component i, $\mathbf{j}$ is the electrical current density, ϕ is the electrical potential, r is the rate of a chemical reaction and $\Delta_r G$ is the reaction Gibb's energy for that process. In the following, many assumptions will be made to simplify the thermodynamics of our system, but it is important to know what exactly these assumptions imply.

First, we are considering a system with constant temperature, so that the temperature gradient ∇T is zero. We assume that the contribution to entropy production due to both the chemical reactions, like hydrolysis (2.6), and the transport of charge (in form of H^+ ions) are negligible compared to that due to mass diffusion, and only consider diffusion of hydrogen in water, i.e. we do not treat water diffusion explicitly. With these assumptions in place, (2.15) reduces to

$$\sigma = -\frac{1}{T}\,\mathbf{J} \cdot (\nabla \mu)_T \;, \tag{2.16}$$

where μ is the chemical potential of hydrogen and the index $_T$ implies derivatives with the temperature held constant. The diffusive flux of hydrogen is then found from (2.14)

$$\mathbf{J}_{\text{diffusion}} = -\frac{L_{\text{HH}}}{T}\,\nabla \mu \,, \tag{2.17}$$

where L_{HH} is the Onsager coefficient for hydrogen mass flux due to a difference in chemical potential in the system. The chemical potential for a dissolved species is[33]

$$\mu = \mu_0 + RT \ln(ac) \,, \tag{2.18}$$

with μ_0 a reference chemical potential, R the gas constant, a the activity coefficient and $c = C_l/C_0$ the concentration of hydrogen dissolved in the liquid relative to a reference state concentration. Applying the gradient operator on (2.18) and using the chain rule gives

$$\begin{aligned}\nabla\mu = RT\nabla\ln(ac) = \frac{RT}{ac}\nabla(ac) = \frac{RT}{ac}\left(c\frac{\partial a}{\partial c}\nabla c + a\nabla c\right)\\ = \frac{RT}{c}\left(1+\frac{c}{a}\frac{\partial a}{\partial c}\right)\nabla c = \frac{RT}{c}\left(1+\frac{\partial \ln a}{\partial \ln c}\right)\nabla c\,.\end{aligned}\tag{2.19}$$

We can finally insert (2.19) into (2.17) to derive the relationship between the diffusive flux and the hydrogen concentration in the liquid,

$$\begin{aligned}\mathbf{J}_{\text{diffusion}} &= -\frac{L_{\text{HH}}}{T}\frac{RT}{c}\left(1+\frac{\partial \ln a}{\partial \ln c}\right)\nabla c\\ &= -D_l\,\nabla C_l\,.\end{aligned}\tag{2.20}$$

But (2.20) is just Fick's first law, and gives the diffusion coefficient as $D_l = \frac{L_{\text{HH}}}{T}\frac{RT}{C_l}\left(1+\frac{\partial \ln a}{\partial \ln c}\right)$, which is thus generally a function of C_l and T. This elucidates the connection between the assumptions made with respect to temperature, chemical reactions and charge transport, and the assumption of no "sources" or "sinks" for hydrogen.

2.2.2 Concentration in the interior of the nanobubble

With the scalar transport and Laplace equations in place as the governing equations for the distribution of hydrogen in the liquid, the next step is to estimate the concentration of hydrogen gas in the interior of the bubble. The Laplace pressure Δp denotes the difference in pressure between the interior and the exterior of a curved surface with principal radii of curvature $\mathcal{R}_1$ and $\mathcal{R}_2$ as

$$\Delta p = p_{\text{int}} - p_{\text{ext}} = \gamma\left(\frac{1}{\mathcal{R}_1}+\frac{1}{\mathcal{R}_2}\right) = \frac{2\gamma}{\mathcal{R}}\,,\tag{2.21}$$

where γ is the surface tension and the last equality holds for spherical surfaces, which have $\mathcal{R}_1 = \mathcal{R}_2 = \mathcal{R}$. We set the interior pressure equal to the gas pressure p_g and assume that the external pressure in the liquid is equal to the atmospheric pressure $p_0 = 101,325\,\text{Pa}$. For a surface which separates hydrogen gas from water, the surface tension is assumed to be that of bulk water at 25°C, namely $7.280\cdot 10^{-2}\,\text{N/m}$. We make the assumption that the hydrogen gas in the nanobubble is uniform and that it behaves ideally, which means that its equation of state is

$$p_g = C_g RT\,,\tag{2.22}$$

where C_g is the concentration of hydrogen gas in the bubble. Insertion of (2.1) and (2.21) into the ideal gas equation gives the hydrogen concentration in the interior of the nanobubble as

$$C_g = \frac{p_g}{RT} = \frac{1}{RT}\left(p_0 + \frac{2\gamma}{\mathcal{R}}\right) = \frac{1}{RT}\left(p_0 + \frac{2\gamma \sin\theta}{r_b}\right). \tag{2.23}$$

2.2.3 Hydrogen flux through nanobubble surface

As described in subsection 2.1.3, the net hydrogen flux across the nanobubble surface must be equal to zero in order for a dynamic equilibrium to be sustained. We thus need to evaluate the integral of the flux given in (2.5), which is a diffusive flux, over the nanobubble surface. Modelling this flux mathematically as a function of the concentrations on the interior and exterior of the surface is a vital element in the verification of the dynamic-equilibrium model, but no serious effort to do so can be found in the literature to the best of the author's knowledge.

We assume that the flux perpendicular to the surface is some function of C_l at the bubble surface and C_g, which allows us to write

$$\mathbf{J} \cdot \hat{\mathbf{n}} \equiv J(C_l, C_g). \tag{2.24}$$

We denote by C_l^* and C_g^* a set of equilibrium values for these hydrogen concentrations, meaning that a system with these values will have zero flux through the surface, i.e. $J(C_l^*, C_g^*) = 0$. A Taylor expansion of the flux around these equilibrium values is then given by

$$J(C_l, C_g) = J(C_l^*, C_g^*) + (C_l - C_l^*)\frac{\partial J(C_l^*, C_g^*)}{\partial C_l} + (C_g - C_g^*)\frac{\partial J(C_l^*, C_g^*)}{\partial C_g} + \dots \tag{2.25}$$

To simplify this expression, we note that there are an infinite amount of sets of equilibrium concentrations. Hence, we set the hydrogen concentration inside the nanobubble to that which we seek equilibrium for ($C_g = C_g^*$), and consider the difference between the hydrogen concentration in the liquid and the equilibrium value C_l^* corresponding to that particular value of C_g. Our expression (2.25) thus becomes

$$J(C_l, C_g) = (C_l - C_l^*)\frac{\partial J(C_l^*, C_g^*)}{\partial C_l} + \mathcal{O}\left((C_l - C_l^*)^2\right), \tag{2.26}$$

so that if we are not too far from equilibrium, a good expression for the flux is

$$J(C_l, C_g) \approx (C_l - C_l^*)\left.\frac{\partial J}{\partial C_l}\right|_{\text{equilibrium}}. \tag{2.27}$$

Henry's law

In 1803, William Henry formulated what has later been named Henry's law:

> At a constant temperature, the amount of a given gas that dissolves in a given type and volume of liquid is directly proportional to the partial pressure of that gas in equilibrium with that liquid.

A mathematical version of this law, which utilizes the proportionality of aqueous and gaseous concentrations instead, is

$$H = \frac{C_l^*}{C_g^*} \,. \tag{2.28}$$

Here, H is the dimensionless Henry's constant, which for hydrogen gas is[34] $H = 1.907 \cdot 10^{-2}$. Inserting (2.28) into (2.27) allows us to approximate the flux through the surface as

$$J = \alpha(C_l - HC_g) \,, \tag{2.29}$$

where we have defined a mass transfer coefficient as $\alpha = \partial J / \partial C_l|_{\text{equilibrium}}$. In principle, α can depend on C_g^* (and C_l^*). The flux assumption (2.29) will be used as our boundary condition at the nanobubble surface, and will also allow us to check the condition of dynamic equilibrium (2.5) since

$$\int_S \mathbf{J} \cdot \hat{\mathbf{n}} \, \mathrm{d}S \propto \int_S (C_l - HC_g) \mathrm{d}S = \int_S C_l \mathrm{d}S - A_S H C_g = 0 \tag{2.30}$$

must hold. The last equality is due to the fact that we do not expect a proportionality constant equal to zero. We have denoted the nanobubble surface area as A_S. The integral in (2.30) must be computed numerically, after which the condition can be checked by demanding that

$$\int_S C_l \mathrm{d}S = A_S H C_g \,. \tag{2.31}$$

2.3 Dissolution time for nanobubbles

2.3.1 Nanobubble literature

Considering the amount of papers written about the superstability of surface nanobubbles, most claims in the literature as to their expected lifetimes are based on extremely simple arguments. Although most papers on nanobubble stability proclaim that the dissolution time should be on the order of microseconds, following classical diffusion theory[10,13,17,20,21], very few contributions even include an equation to support this statement. The main argument is that of Seddon et al.[16], who state that the dissolution time, or lifetime, is

$$t_l \approx \frac{\mathcal{R}_0^2}{D_l} \,, \tag{2.32}$$

where $\mathcal{R}_0$ is the initial bubble radius of curvature. But since no citations are given as to what these "simple arguments from classical diffusion theory" are, this seems to be a statement based simply on dimensional analysis. It does not take into consideration that the bubbles are on a surface, or the effect of impurities or the dynamic-equilibrium arguments. Even in the consideration of a bulk nanobubble, this argument is extremely simplistic. Weijs et al.[22] claim that the relevant length scale is the distance from the bubble to the ambient air surroundings, stating that this gives a lifetime of approximately

10^5 s. Introducing such vague length-scale arguments is too narrow a view, even if it gives a lifetime closer to observed values. Instead, a more thorough model is needed for which the observed lifetimes appear less surprising. It should be stressed that all analytical and numerical models presented give lower bounds on the lifetimes of bulk nanobubbles. Since surface nanobubbles are being studied, the arguments presented earlier lead us to expect even longer lifetimes.

2.3.2 Analytical solution

A model for the lifetime of gas bubbles in liquids, which has received no attention in the nanobubble stability debate, was published as early as 1950 [35]. In a paper by Ljunggren et al. from 1997 [36], an improved analytical expression for the lifetime of small bubbles was presented, which we introduce here for comparison with our results. The reader is advised that simple Laplace transforms will take place, and a brief introduction to this method can be found in appendix A. We wish to calculate the lifetime t_l of a hydrogen nanobubble submerged in water. We assume that the bubble exists in an infinitely large aqueous volume, and that the hydrogen concentration tends toward zero when we are sufficiently far from the bubble. A hydrogen concentration in the bulk liquid which is higher than zero would lead to a longer lifetime for the bubble. With a spherical bubble of radius $\mathcal{R}(t)$, the problem is isotropic, and thus has no angular dependency. Figure 2.8 illustrates how the bubble size is modelled as a function of the spherical radius.

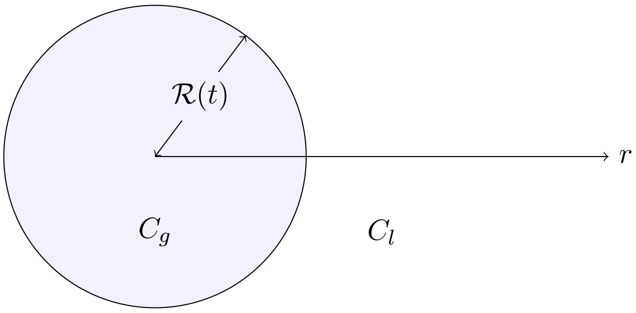

Figure 2.8: Illustration of a bulk bubble.

We start with the scalar transport equation (2.11) but disregard the advective term, assuming it will be small compared to the diffusive one. In spherical coordinates, we thus have

$$\dot{C}_l = D_l \Delta C_l = D_l \left(\frac{2}{r} \partial_r C_l + \partial_r^2 C_l \right) . \tag{2.33}$$

By introducing

$$x = r - \mathcal{R}(t)$$

and

$$u(x,t) = r C_l(r,t) ,$$

a PDE of the exact same form as Fick's second law emerges, i.e.

$$\dot{u} = D_l \partial_x^2 u \,. \tag{2.34}$$

It is important to emphasize, however, that the PDE should be solved on a domain which changes in size since the bubble is shrinking, which is not taken into consideration in this model. The initial and boundary conditions are

$$u(0,t) \equiv \psi(t) = \mathcal{R}(t) C_l(\mathcal{R}(t), t) \,, \tag{2.35a}$$

$$u(x \to \infty, t) = 0 \,, \tag{2.35b}$$

$$u(x, 0) = 0 \,. \tag{2.35c}$$

In other words the concentration at the bubble surface ($x = 0$) is described by some function of time only, the concentration far away is zero, and the initial concentration in the liquid is zero. Taking the Laplace transform of (2.34) - (2.35) with p the Laplacian variable then yields

$$\partial_x^2 \bar{u}(x,p) - \frac{p}{D_l} \bar{u}(x,p) = 0 \tag{2.36a}$$

$$\bar{u}(0,p) = \bar{\psi}(p) \,. \tag{2.36b}$$

The general solution of (2.36) is

$$\bar{u}(x,p) = \bar{\psi}(p) e^{-x\sqrt{p/D_l}} \,,$$

from which, by taking the inverse Laplacian, we find the general solution

$$u(x,t) = \psi(t) * \mathcal{L}\left\{ e^{-x\sqrt{p/D_l}} \right\} = \frac{x}{2\sqrt{\pi D_l}} \int_0^t \frac{\psi(t-\tau)}{\tau^{3/2}} e^{-\frac{x^2}{4D_l\tau}} \mathrm{d}\tau \,. \tag{2.37}$$

It should be stressed once more that the convective term has been neglected and a time-independent domain is considered. After finding the general solution as stated in (2.37), Ljungren et al. go on to argue that if Henry's law can be assumed to hold, then

$$C_g(t) = \frac{1}{H} C_l(\mathcal{R}(t), t) \,,$$

but this is only true if the system is in (chemical) equilibrium! Since there is a net flux across the surface, this is obviously not the case. This discrepancy represents the largest difference between our model and that of Ljunggren et al. With this equilibrium assumption in place, and recalling (2.23), we can set

$$\psi(t) = H C_g \mathcal{R} = \frac{H}{RT} \left(p_0 \mathcal{R} + 2\gamma \right) \approx \frac{2\gamma H}{RT} \,,$$

where the last assumption holds if $\mathcal{R} << 2\gamma/p_0 = 1.46\,\mu\text{m}$, i.e. if the bubble is small enough. With this time-independent boundary condition, the solution becomes[36]

$$u(x,t) = \frac{4\gamma H}{RT\sqrt{\pi}} \int_{\frac{x}{2\sqrt{D_l t}}}^{\infty} e^{-\xi^2}\mathrm{d}\xi\,,$$

where $\xi = \frac{x}{2\sqrt{D_l \tau}}$. Since $u = rC_l$ and $x = r - \mathcal{R}$, we get

$$C_l(x,t) = \frac{4\gamma H}{RT(x+\mathcal{R})\sqrt{\pi}} \int_{\frac{x}{2\sqrt{D_l t}}}^{\infty} e^{-\xi^2}\mathrm{d}\xi\,.$$

Finally, by differentiation, the flux at the boundary becomes

$$\left.\frac{\partial C_l}{\partial x}\right|_{x=0} = -\frac{2\gamma H}{RT\mathcal{R}}\left(\frac{1}{\mathcal{R}} + \frac{1}{\sqrt{\pi D_l t}}\right)\,.$$

As is shown by mass conservation at the interface ($x = 0$) in appendix B, the connection between the boundary flux and the rate of change of the bubble radius is

$$D_l\left.\frac{\partial C_l}{\partial x}\right|_{x=0} = \frac{1}{RT}\left(p_0 + \frac{4\gamma}{3\mathcal{R}}\right)\dot{\mathcal{R}}\,.$$

Neglecting the atmospheric pressure once more, we now have

$$\dot{\mathcal{R}} = -\frac{3}{2}D_l H\left(\frac{1}{\mathcal{R}} + \frac{1}{\sqrt{\pi D_l t}}\right)\,,$$

or, recognizing the temporal derivative of $\mathcal{R}^2$,

$$2\mathcal{R}\dot{\mathcal{R}} = \frac{\mathrm{d}}{\mathrm{d}t}\mathcal{R}^2 = -3D_l H\left(1 + \frac{\mathcal{R}}{\sqrt{\pi D_l t}}\right)\,.$$

To find an analytical solution, the additional assumption of $\mathcal{R} << \sqrt{\pi D_l t}$ is made, which must hold after some initial phase. For $t = 1\,\mu\text{s}$, we have $\sqrt{\pi D_l t} \approx 120\,\text{nm}$. This simplification is also an important assumption which differentiates this model from the one developed in this thesis. Finally, the expression for the relative bubble radius $\eta(t) = \mathcal{R}(t)/\mathcal{R}_0$ as a function of time becomes

$$\eta^2(t) = 1 - \frac{3D_l H}{\mathcal{R}_0^2}t \tag{2.38}$$

The lifetime of the bubble, i.e. the time it takes for the bubble radius to become zero, is then

$$t_l = \frac{\mathcal{R}_0^2}{3D_l H}\,. \tag{2.39}$$

While the inverse scaling with D_l is intuitive, the scaling proportional to the initial surface area rather than the initial volume is not.

2.3.3 Mean-field model

Another interesting approach was shown by Kimmerle[37]. A mean-field model for multiple bulk and surface nanobubbles was implemented in order to simulate the dissolution time, resulting in lifetimes of several orders of magnitude larger than those put forth in the nanobubble literature. The dissolution times were calculated by considering a quasi-static equilibrium obtained by interaction of the hydrogen bubbles through a mean hydrogen concentration in the solute. It indicates that the long lifetimes of nanobubbles, observed experimentally, might be the result of a collective interaction between a multitude of bubbles. In other words, a single-bubble analysis might not explain the dynamics of an ensemble of bubbles.

2.4 Numerical methods

Many boundary value problems (BVPs) for partial differential equations (PDEs) cannot be solved analytically, and numerical methods for approximating their solutions are necessary. A short introduction to the methods employed are given here, while a little more theoretical background is provided in appendix C.

2.4.1 The finite-element method

The finite-element method (FEM) is a numerical method which uses the calculus of variations to produce a stable approximation of a solution to an ODE or a PDE, while minimizing the error between a sought solution and its approximation. It connects a large number of discrete subdomains to approximate a larger one. The subdomains are referred to as finite elements, hence the method's name.

Since FEM has been used in three dimensions in this project, the method has been explained from a 3D viewpoint in appendix C, but it can be used in one and two dimensions as well as any higher number of dimensions as long as the necessary conditions are fulfilled. The Laplace equation is used as an example throughout the explanation of the method, since it is the relevant equation for the diffusion of hydrogen in water at dynamic equilibrium (with load functions equal to zero). The procedures for Dirichlet, Neumann and Robin boundary conditions are all included in the derivation.

To solve a partial differential equation on a 3D domain using FEM, a mesh is generated on the domain. The mesh is connected by its coordinate points, and an element in the mesh is tetrahedral, with four of the mesh points as its vertices. Appendix C explains how FEM transforms a continuous BVP for PDEs to a finite set of linear equations, ready to be solved numerically as a matrix equation. A short note on the implementation of Gaussian quadrature and the trapezoidal rule for solving integrals numerically is also provided in appendix C. For an in-depth study of the finite-element method and its applications, Quarteroni's book[38] is an excellent resource.

2.4.2 The finite-difference method

Another common method for approximating differential equations numerically is based on finite differences. In many ways it is simpler than FEM, and as we apply it to a one-dimensional problem in this thesis, the short derivation of difference formulae based on Taylor's formula given in appendix C should suffice for the reader to follow our model.

Chapter 3

Problem descriptions and numerical schemes

3.1 Steady-state model for surface nanobubbles

3.1.1 System description

The goal for this numerical model is to investigate the validity of the dynamic-equilibrium hypothesis by investigating whether a nanobubble can be held at a stable size if it is replenished with hydrogen gas through electrolysis. We therefore model a steady-state bubble with a given bubble geometry, and analyse for what magnitude of the electrolysis current J_0 and mass transfer coefficient α the condition for dynamic equilibrium given by (2.5) is fulfilled. The system contains a single nanobubble with radius r_b generated on a platinum disc of radius r_d, inspired by the experimental achievements of Luo et al.[8] We consider a test region filled with water and allow for electrolysis at a platinum disc. Figure 3.1 shows the system set-up. We have conducted simulations in both two and three dimensions, and as such explain the domain composition for both cases. Although the three dimensional model is obviously more precise, some qualitative results are easier shown using the 2D model. Figures 3.2-3.4 exhibit the generated meshes for the domains and can be helpful to obtain an intuitive understanding of the following definitions.

2D domain

Our two-dimensional domain Ω^{2D} is the shape of a square with side lengths L minus the projection of the nanobubble, within which we seek to find the distribution of hydrogen gas. In this square, the horizontal position is denoted by r and the vertical position by z, both of which are strictly positive since we are considering a symmetric half-cell. We need to clearly define the different regions of the domain boundary $\partial\Omega^{\mathrm{2D}}$. The edges furthest from the bubble represent a location far enough from the electrode to be independent of the

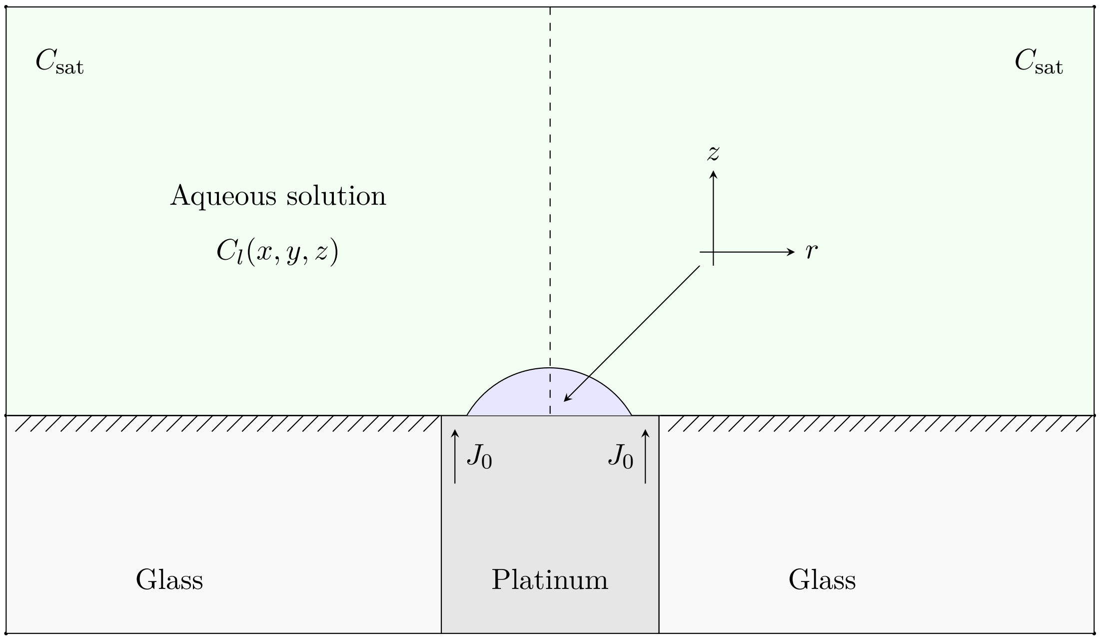

Figure 3.1: Illustration of physical model used for steady-state calculations. A single nanobubble is sustained on a platinum disc with a constant electron flux per unit area J_0. Electrolysis occurs on the part of the platinum surface not covered by the nanobubble, and affects the hydrogen concentration C_l in the remaining liquid. There is no flux across the glass surface, the flux through the bubble surface is modelled by a Robin condition, and the concentration is held at the hydrogen saturation concentration sufficiently far from the nanobubble.

bubble and electrode dynamics, and we therefore enforce a Dirichlet boundary condition by setting the concentration equal to the saturation concentration C_{sat}. Mathematically, the surface is

$$\partial\Omega^{\text{2D}}_{\text{sat}} : z = L \text{ or } r = L \,.$$

Note that r denotes the radial distance from a straight line through the bubble apex, while z is the height above the electrode surface. The second boundary region to consider is that of the active platinum electrode surface. This is where the supplied current facilitates hydrogen production, yielding a constant diffusive normal flux. The boundary condition here is of Neumann type. It lies in the plane $z = 0$ and is bounded by the platinum disc radius on the outer side and the nanobubble radius on the inner one. We thus define it by

$$\partial\Omega^{\text{2D}}_{\text{Pt}} : \begin{cases} r_b < r \leq r_d \\ z = 0 \end{cases} \,.$$

Next we consider the bubble surface, where a Robin boundary condition is implemented. If the bubble has radius of curvature $\mathcal{R}$ and maximum height h_b over the electrode surface, it is given by

$$\partial\Omega^{\text{2D}}_{\text{bubble}} : r^2 + (z + \mathcal{R} - h_b)^2 = \mathcal{R}^2 \,.$$

Finally, we need to define the zero flux Neumann boundary. This boundary is in fact the union of two smaller boundaries, one where the flux is zero because it consists of glass, and the other where it is zero due to angular independency, above the bubble apex. Let us define the former as

$$\partial\Omega^{\mathrm{2D}}_{\mathrm{glass}} : \begin{cases} r_d < r \leq L \\ z = 0 \end{cases} ,$$

which includes the whole bottom part of the system boundary except for the platinum disc. Our last boundary edge, directly above the bubble apex, is

$$\partial\Omega^{\mathrm{2D}}_{\mathrm{apex}} : \begin{cases} z > h \\ r = 0 \end{cases} .$$

3D domain

When we move to three dimensions, we consider a hemisphere of radius L instead and denote a point in space by standard Cartesian coordinates. Since we are considering the entire hemisphere, there is no boundary above the bubble apex, but apart from that the boundary surface is defined similarly to the boundary edge in 2D. Our domain is referred to as Ω^{3D}, and its boundary $\partial\Omega^{\mathrm{3D}}$ is composed of

$$\partial\Omega^{\mathrm{3D}}_{\mathrm{sat}} : \; x^2 + y^2 + z^2 = L^2 ,$$

$$\partial\Omega^{\mathrm{3D}}_{\mathrm{Pt}} : \begin{cases} r_b^2 < x^2 + y^2 \leq r_d^2 \\ z = 0 \end{cases} ,$$

$$\partial\Omega^{\mathrm{3D}}_{\mathrm{bubble}} : \; x^2 + y^2 + (z + \mathcal{R} - h_b)^2 = \mathcal{R}^2 ,$$

$$\partial\Omega^{\mathrm{3D}}_{\mathrm{glass}} : \begin{cases} r_d^2 < x^2 + y^2 \leq L^2 \\ z = 0 \end{cases} .$$

In the following, we will explain the model for the three-dimensional case. The analogy to two dimensions follows immediately. As such, we will drop the 3D-superscript when denoting domain areas.

3.1.2 Problem statement

For a given system geometry and nanobubble radius, we wish to find the particle flux J_0 required to keep the bubble in dynamical equilibrium. This value will also depend on the mass transfer coefficient α, which is another important system parameter. Using (2.12), (2.20), (2.29) and (3.7) the system to be analysed with FEM can be set up in the following manner[1]:

$$\Delta C_l = 0 \qquad \text{in} \quad \Omega \tag{3.1a}$$

$$C_l = C_{\text{sat}} \qquad \text{on} \quad \partial\Omega_{\text{sat}} \tag{3.1b}$$

$$\frac{\partial C_l}{\partial n} = -\frac{J_0}{D_l} \qquad \text{on} \quad \partial\Omega_{\text{Pt}} \tag{3.1c}$$

$$C_l + \frac{D_l}{\alpha}\frac{\partial C_l}{\partial n} = HC_g \qquad \text{on} \quad \partial\Omega_{\text{bubble}} \tag{3.1d}$$

$$\frac{\partial C_l}{\partial n} = 0 \qquad \text{on} \quad \partial\Omega_{\text{glass}} \tag{3.1e}$$

As seen from (3.1c), J_0 is needed to calculate the Neumann boundary condition at the flux boundary. This means that after solving the system (3.1) for a given value of α, we need to check the condition for dynamic equilibrium given by (2.31), adjust the flux accordingly, and iterate on the calculations until a satisfactory result is obtained.

Nondimensionalization

We introduce dimensionless spacial coordinates (ξ, η, ζ) through division of our standard Cartesian coordinates (x, y, z) by the system length L. The dimensionless hydrogen concentration in the liquid is given by the ratio of the actual concentration to the hydrogen saturation concentration $C_{\text{sat}} = 0.8\,\text{mol/m}^3$, i.e. $c = C_l/C_{\text{sat}}$. Substituting this into (3.1) gives the dimensionless set of equations:

$$\Delta c = 0 \qquad \text{in} \quad \Omega \tag{3.2a}$$

$$c = 1 \qquad \text{on} \quad \partial\Omega_{\text{sat}} \tag{3.2b}$$

$$\frac{\partial c}{\partial n} = -\frac{L}{C_{\text{sat}}}\frac{J_0}{D_l} \qquad \text{on} \quad \partial\Omega_{\text{Pt}} \tag{3.2c}$$

$$c + \frac{D_l}{\alpha L}\frac{\partial c}{\partial n} = H\frac{C_g}{C_{\text{sat}}} \qquad \text{on} \quad \partial\Omega_{\text{bubble}} \tag{3.2d}$$

$$\frac{\partial c}{\partial n} = 0 \qquad \text{on} \quad \partial\Omega_{\text{glass}} \tag{3.2e}$$

---

[1] The zero-flux condition in 2D corresponding to (3.1e) is implemented on $\partial\Omega^{\text{2D}}_{\text{glass}} \cup \partial\Omega^{\text{2D}}_{\text{apex}}$

3.1.3 Discretization

Mesh generation

As described earlier, the test volume is modelled by a square mesh in 2D and a hemispherical one in 3D. Since we require much more finer mesh structure near the region where the nanobubble exists than further out towards the boundary, and because our domain decomposition is non-trivial, we generate meshes using DistMesh[39], a simple mesh generator that describes the mesh shape and nodal spacing by distance functions. Figure 3.2 shows a 2D mesh with boundary edges, while figures 3.3 and 3.4 illustrate the 3D meshes and their boundary surfaces.

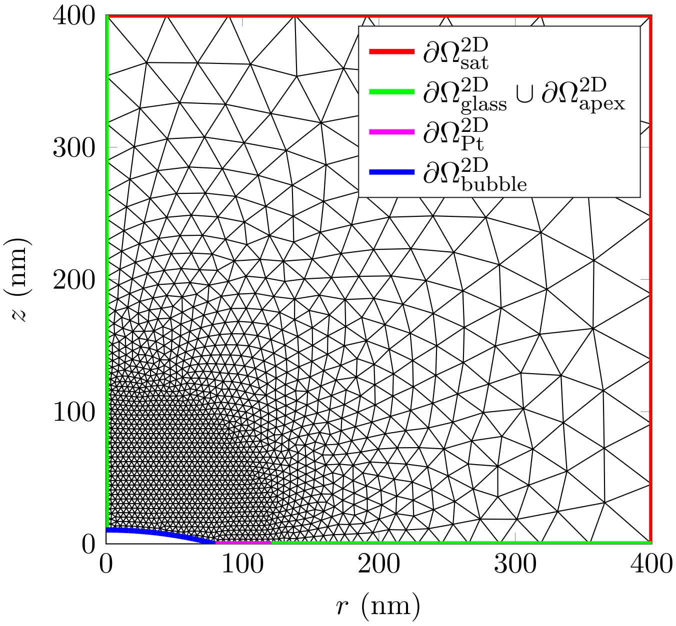

Figure 3.2: Example of 2D mesh with $\theta = 15°$, including the decomposition of the boundary edge $\partial\Omega^{2D}$.

(a) Top surface: $\partial\Omega^{3D}_{sat}$

(b) Interior of domain: Ω^{3D}

Figure 3.3: Example of 3D mesh with $\theta = 15°$, showing (a) the top surface seen from the outside and (b) the interior of the domain. The density of node points in the mesh is greatly reduced far from the bubble.

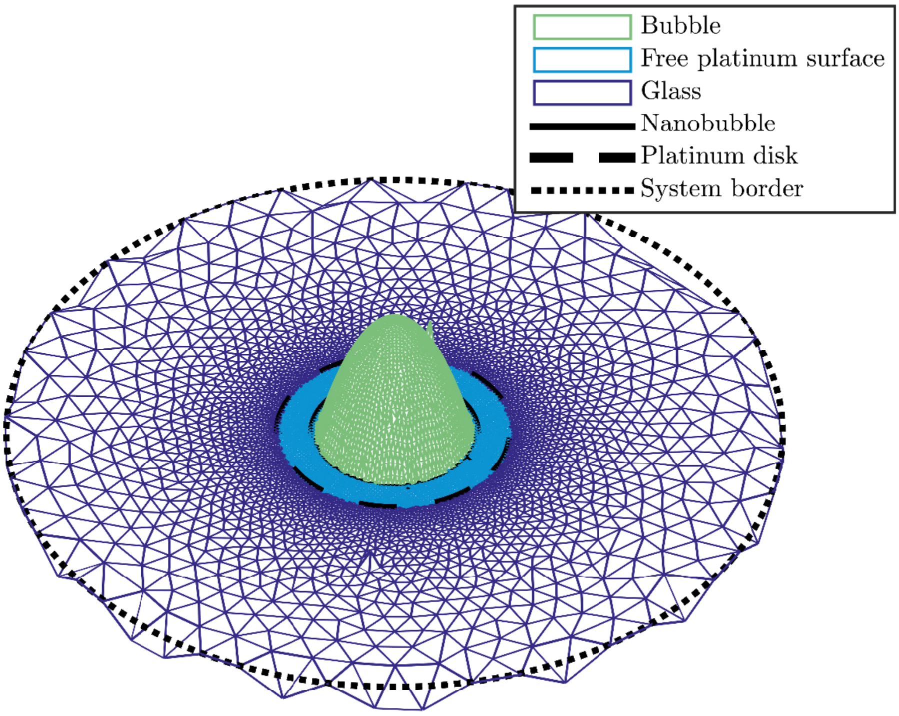

Figure 3.4: Close-up of the bottom part of the domain boundary in 3D. Note that the ratio of the nanobubble height to the radial distance is not to scale; the z-axis has been greatly stretched to clearly show the boundary decomposition.

Stiffness matrix and load vector

With the mesh generated, we build the stiffness matrix $\mathbf{A}$ and load vector $\mathbf{b}$ using (C.11) and (C.13). Since MATLAB is excellent at matrix operations but has very high computational times for large for-loops, these processes are vectorised by noting that the numerical integrals can be evaluated by geometrical considerations. For example, the first term in the local stiffness matrix for an element given by (C.4) can be written

$$\frac{1}{(3!)^2 \cdot V} \mathbf{n}_i \cdot \mathbf{n}_j \,,$$

where V is the volume of the element and $\mathbf{n}_i$ is the inward unit normal of the face opposite the vertex at (x_i, y_i, z_i). This is due to the fact that $\nabla \phi_i$ is a normal vector to that face, and that $\phi_i(\mathbf{x}) = \mathbf{0}$ for all $\mathbf{x}$ on the face. The gradient is thus given by

$$\nabla \phi_i = \frac{1}{3! \cdot V} \mathbf{n}_i \,.$$

Building a sparse matrix with elements like those described above, is elegantly done using MATLAB's `sparse` function. The same type of vectorization can be applied to generate the load vector $\mathbf{b}$, but from (3.2a) we have that $f = 0$, so the load vector is equal to zero except at the boundary nodes.

Boundary conditions

By applying the finite-element method to (3.2), the boundary conditions are automatically implemented in the weak formulation as explained in appendix C. The boundary conditions of Dirichlet (3.2b) and Robin type (3.2d) give contributions to the stiffness matrix. The Dirichlet condition is implemented by initializing the concentration vector **c** to zero everywhere except at the relevant nodes, where it is set to unity according to (3.2b). We then calculate the Robin contribution by vectorized Gaussian quadrature, completing the assembly of **A** including boundary conditions. When solving the matrix equation (C.10), we will only do so for the non-Dirichlet nodes, thus automatically including the lifting function R_g. Note that all this happens only once during the simulation, since the variable system parameter J_0 only appears in (3.2c). The contribution from the Robin condition to the load vector is only computed once also, and the load vector contributions too are included by vectorized numerical quadrature.

3.1.4 Computational algorithm

After solving the system of equations for a given α, the concentration $c(\xi, \eta, \zeta)$ at each node of the mesh is stored in the concentration vector **u**. It is important to note that we have now found the concentration in the test volume given a test flux J_0. To find out how well this flux matches the one required to sustain stable equilibrium, we need to find the value of the integral in (2.31). We estimate the integral numerically over the curved boundary surface $\partial\Omega_{\text{bubble}}$ using the trapezoidal rule. We denote the numerical and theoretical values of the integral I_N and I_T, respectively, i.e.

$$I_N = \int_S C_l \mathrm{d}S \,, \tag{3.3}$$

$$I_T = A_S H C_g \,. \tag{3.4}$$

For the flux of a system to be satisfactory, we require the absolute value of the relative error ε less than some small tolerance tol, i.e.

$$|\varepsilon| = \frac{|I_N - I_T|}{I_T} \leq tol \,. \tag{3.5}$$

To reach dynamic equilibrium for a given nanobubble geometry and mass transfer coefficient, we thus solve the FEM system with a test value for the flux, compute the numerical integral, and subsequently increase or decrease the flux by adding a term proportional to ε. In order to obtain rapid convergence, we continuously trace the error and update the proportionality factor κ according to algorithm 1 below. The process is repeated until ε is sufficiently small, at which point we assign the value J_0 as the dynamic equilibrium molar flux for the system. In principle, we are solving the free boundary problem ”for what geometry and flux is the nanobubble stable for a given α?” by doing the reciprocal calculations, as stated in algorithm 2 below. A last trick for reducing the computational time is that when we compute J_0 for many increasing values of α, we guess J_0 based on the previous run and initiate κ at its previous final value.

```
Data: $\varepsilon$, $\varepsilon_{\text{previous}}$
Result: $\kappa$
if $\varepsilon/\varepsilon_{\text{previous}} > 1$ then
    $\kappa = -\kappa$;
end
if $|\varepsilon/\varepsilon_{\text{previous}}| > 1$ then
    $\kappa = \kappa/3$;
else
    if $|\varepsilon/\varepsilon_{\text{previous}}| > 0.3$ then
        $\kappa = 3\kappa$;
    end
end
```

Algorithm 1: Altering the proportionality constant based on current and previous errors.

```
Data: Mesh of bubble geometry, $\alpha$, $tol$, physical constants
Result: $J_0$
calculate $I_T$ from (3.4);
build $\mathbf{A}$ from (3.2a), (3.2d) and (C.11);
initialize $\mathbf{u}$ with zeros except according to (3.2b);
build $\mathbf{b}$ from (3.2d) and (C.13);
initialize $\varepsilon > tol$;
while $\varepsilon > tol$ do
    add $J_0$-dependent part to $\mathbf{b}$ from (3.2c) and (C.13);
    solve $\mathbf{A} \cdot \mathbf{u} = \mathbf{b}$ for free nodes;
    calculate $I_N$ using Gaussian quadrature and $\varepsilon$ from (3.5);
    optimize $\kappa$ using algorithm 1;
    $J_0 = J_0 - \kappa\varepsilon$;
end
```

Algorithm 2: Determination of equilibrium flux for steady-state nanobubble system.

3.1.5 System parameters

The system parameters shown in table 3.1 have been used except where specified otherwise. The disc radius r_d is 50% larger than that of the nanobubble, which ensures that most of the electrode is covered while leaving some area for electrolysis. L, which is the radius of the hemisphere that makes up the domain Ω, is chosen large enough to prevent the saturation concentration C_{sat} from being dominant in the system. The choice for the contact angle is a typical value for surface nanobubbles in experiments. The temperature is 25 °C to mimic room temperature, while the diffusion coefficient D_l for hydrogen in water is the experimental value under the thermodynamic assumptions discussed in subsection 2.2.1. Since a higher mesh resolution gives more accurate results, the amount of nodes is as high as possible without the runtime getting out of control. With this mesh size, a single FEM simulation in 3D typically takes two minutes, which we deem tolerable. For the 2D model, the runtime is only a fraction of a second.

Table 3.1: Default parameters for steady-state model

L/r_b	r_d/r_b	θ	T	D_l	tol	Node points		Elements	
[−]	[−]	[°]	[K]	[m^2/s]	[−]	2D	3D	2D	3D
5	1.5	15	298	$4.5 \cdot 10^{-9}$	10^{-7}	1,568	111,468	3,021	656,620

3.2 Lower bound on lifetime of bulk nanobubbles

3.2.1 System description

In a second part of this thesis, we wish to calculate a lower bound for the lifetime t_l of a bulk hydrogen nanobubble submerged in water. Our assumptions are that the system is isothermal at temperature T and in mechanical equilibrium, and we assume that the molar flux J perpendicular to the bubble surface can be approximated by (2.29). Note that $\hat{\mathbf{n}} = -\hat{\mathbf{r}}$ is directed towards the interior of the bubble, so that we have a positive flux for $C_l > HC_g$. In the liquid, the generic scalar transport equation without sources or sinks (2.11) holds. We also assume that the bubble exists in an infinitely large aqueous volume, and that the initial hydrogen concentration is zero in the liquid. Sufficiently far from the bubble, a boundary condition is imposed in order to keep the amount of hydrogen molecules in the system constant. With a spherical bubble of radius $\mathcal{R}(t)$, the problem is isotropic, and thus has no angular dependency. The model is similar to that of Ljunggren et al., used to find an analytical solution[36], but it is more thorough since it takes into consideration the growing domain on which the PDE is solved. It also includes the term due to advection and incorporates Henry's law in a proper manner. Many of the steps in the derivation of this model have been moved to appendix B for readability.

Liquid velocity

To include the advective term in (2.11), we need to describe the velocity $\mathbf{v}_l$ of the liquid itself. As we show in appendix B, an appropriate assumption is

$$\mathbf{v}_l = \frac{\mathcal{R}^2}{r^2}\dot{\mathcal{R}}\,\hat{\mathbf{r}}\ , \tag{3.6}$$

so that the advective term becomes

$$-\nabla\cdot(\mathbf{v}_l C_l) = -\frac{\mathcal{R}^2}{r^2}\dot{\mathcal{R}}\,\partial_r C_l\,.$$

Mass balance at interface

In appendix B, we derive by mass balances at the interface ($r=\mathcal{R}$) that the flux through the bubble surface is given by

$$J = D_l\partial_r C_l = \frac{1}{RT}\left(p_0+\frac{4\gamma}{3\mathcal{R}}\right)\dot{\mathcal{R}}\,. \tag{3.7}$$

We equate these two different expressions for J with (2.29) in order to find both the interfacial boundary condition for C_l and an ODE for $\mathcal{R}$.

Conservation of hydrogen

In order to have the same amount of hydrogen molecules in the system at all times, we derive a boundary condition at some large radial value $r = r_{\max}$ which is given by

$$C_l - \left(\frac{r_{\max}}{\mathcal{R}}\right)^2\frac{D_l}{\dot{\mathcal{R}}}\partial_r C_l = 0\,. \tag{3.8}$$

This derivation is also given in appendix B.

3.2.2 Problem statement

PDE for hydrogen concentration in liquid

With the assumptions as outlined above, noting especially the equations (3.6)-(3.8), the following is a valid formulation of our PDE.

$$\dot{C}_l - D_l\Delta C_l + \frac{\mathcal{R}^2}{r^2}\dot{\mathcal{R}}\partial_r C_l = 0 \qquad \text{on} \quad r>\mathcal{R} \tag{3.9a}$$

$$C_l - \left(\frac{r_{\max}}{\mathcal{R}}\right)^2\frac{D_l}{\dot{\mathcal{R}}}\partial_r C_l = 0 \qquad \text{at} \quad r=r_{\max} \tag{3.9b}$$

$$C_l - \frac{D_l}{\alpha}\partial_r C_l = HC_g \qquad \text{at} \quad r=\mathcal{R} \tag{3.9c}$$

$$C_l(r,0) = 0 \qquad \text{on} \quad r>\mathcal{R} \tag{3.9d}$$

ODE for bubble radius

To obtain the bubble radius' temporal dependency $\mathcal{R}(t)$, we equate the left-hand side of (3.7) with (2.29), i.e.

$$\frac{1}{RT}\left(p_0 + \frac{4\gamma}{3\mathcal{R}}\right)\dot{\mathcal{R}} = \alpha(C_l(\mathcal{R},t) - HC_g(\mathcal{R}))\,. \tag{3.10}$$

Noting that

$$\frac{1}{RT}\left(p_0 + \frac{4\gamma}{3\mathcal{R}}\right) = C_g(\mathcal{R}) - \frac{1}{RT}\frac{2\gamma}{3\mathcal{R}}\,,$$

and dividing (3.10) by this expression gives

$$\dot{\mathcal{R}} = -\alpha\,\frac{HC_g(\mathcal{R}) - C_l(\mathcal{R},t)}{C_g(\mathcal{R}) - \frac{1}{RT}\frac{2\gamma}{3\mathcal{R}}}\,, \tag{3.11a}$$

which is an ODE for $\mathcal{R}(t)$, completed by the initial condition

$$\mathcal{R}(0) = \mathcal{R}_0\,. \tag{3.11b}$$

It couples to the liquid only through the hydrogen concentration in the liquid at the surface, $C_l(\mathcal{R},t)$.

Domain mapping

Since the bubble radius enters into the PDE (3.9) which determines the hydrogen concentration in the liquid, and the hydrogen concentration at the boundary enters into the ODE (3.11) for the radius, we need to perform iterations of both equations for each time step and couple the results. Before we discretize the equations, however, we need to address a difficulty with the PDE, namely the time-dependency of the spatial domain Ω. When the bubble has radius $\mathcal{R}(t)$, and we set $r_{\max}$ as the largest distance from the bubble center to be considered, the domain is

$$\Omega(t) = [\mathcal{R}(t), r_{\max}] \times [0,\pi) \times [0,2\pi)\,.$$

We wish to use the same grid $\Omega(0)$ to represent $\Omega(t)$ at all times, so we need to introduce a transformation $\Phi : \Omega(0) \to \Omega(t)$. We want the transformation to behave so that $\mathcal{R}(t) < r < r_{\max}$ and $\mathcal{R}_0 < \tilde{r} < r_{\max}$, which means that the far end of the time-dependent domain is held fixed while the starting point is stretched like a rubber band as the bubble radius shrinks. Figure 3.5 illustrates the radial stretching.

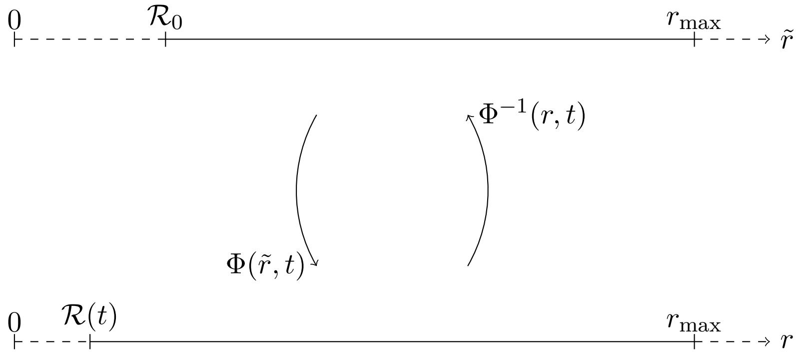

Figure 3.5: Rubber-band transformation from constant to time-dependent domain

It is clear that the domain is stretched by a factor

$$s(t) = \frac{r_{\max} - \mathcal{R}}{r_{\max} - \mathcal{R}_0}\,. \tag{3.12}$$

A detailed explanation of the domain mapping is given in appendix B.

Transformation of PDE

The hydrogen concentration in the liquid in our reference domain is denoted $\tilde{C}_l$ and the derivation given in appendix B allows us to rewrite the PDE (3.9) in the transformed coordinate system.

$$\dot{\tilde{C}}_l + \frac{1}{s}\left(\left(\frac{\mathcal{R}}{s\tilde{r} - (s-1)r_{\max}}\right)^2 - \frac{r_{\max} - \tilde{r}}{r_{\max} - \mathcal{R}_0}\right)\dot{\mathcal{R}}\,\partial_{\tilde{r}}\tilde{C}_l$$

$$-\frac{D_l}{s^2}\left(\frac{2s}{s\tilde{r} - (s-1)r_{\max}}\,\partial_{\tilde{r}}\tilde{C}_l + \partial_{\tilde{r}}^2\tilde{C}_l\right) = 0 \qquad \text{on } \tilde{r} > \mathcal{R}_0 \tag{3.13a}$$

$$\tilde{C}_l - \frac{1}{s}\left(\frac{r_{\max}}{\mathcal{R}}\right)^2 \frac{D_l}{\dot{\mathcal{R}}}\partial_{\tilde{r}}\tilde{C}_l = 0 \qquad \text{at } \tilde{r} = r_{\max} \tag{3.13b}$$

$$\tilde{C}_l - \frac{1}{s}\frac{D_l}{\alpha}\,\partial_{\tilde{r}}\tilde{C}_l = HC_g \qquad \text{at } \tilde{r} = \mathcal{R}_0 \tag{3.13c}$$

$$\tilde{C}_l(\tilde{r},0) = 0 \qquad \text{on } \tilde{r} > \mathcal{R}_0 \tag{3.13d}$$

Nondimensionalization

To obtain the ODE and PDE in dimensionless form, we introduce the dimensionless variables $\tau = t/t_0$, $\rho = \tilde{r}/\mathcal{R}_0$, $c = \tilde{C}_l/C_0$ and $\eta = \mathcal{R}/\mathcal{R}_0$. The constants are given by $t_0 = \frac{\mathcal{R}_0^2}{D_l}$ and $C_0 = \frac{2\gamma}{RT\mathcal{R}_0}$. We also introduce, for simplicity, the dimensionless constant

$\nu = \frac{D_l}{\alpha \mathcal{R}_0}$. The ODE for the bubble radius thus becomes

$$\partial_\tau \eta = -\frac{1}{\nu} \frac{Hc_g - c(1,\tau)}{c_g - \frac{1}{3\eta}}\,, \tag{3.14a}$$

$$\eta(0) = 1\,, \tag{3.14b}$$

where

$$c_g(\eta) = \frac{C_g}{C_0} = \frac{p_0 R_0}{2\gamma} + \frac{1}{\eta}\,. \tag{3.15}$$

Similarly, we get the dimensionless PDE:

$$\partial_\tau c + \frac{1}{s}\left(\left(\frac{\eta}{s\rho - (s-1)\rho_{\max}}\right)^2 - \frac{\rho_{\max} - \rho}{\rho_{\max} - 1}\right)\partial_\tau \eta \partial_\rho c$$

$$-\frac{1}{s^2}\left(\frac{2s}{s\rho - (s-1)\rho_{\max}}\partial_\rho c + \partial_\rho^2 c\right) = 0 \qquad \text{on}\, \rho > 1 \tag{3.16a}$$

$$c - \frac{1}{s}\left(\frac{\rho_{\max}}{\eta}\right)^2 \frac{\partial_\rho c}{\partial_\tau \eta} = 0 \qquad \text{at}\, \rho = \rho_{\max} \tag{3.16b}$$

$$c - \frac{1}{s}\nu \partial_\rho c = Hc_g \qquad \text{at}\, \rho = 1 \tag{3.16c}$$

$$c(\rho, 0) = 0 \qquad \text{on}\, \rho > 1 \tag{3.16d}$$

3.2.3 Discretization

Spatial and temporal discretization

Finite differences, briefly explained in appendix C, are implemented in order to discretize the dimensionless differential equations. We introduce the $M+2$ spatial points ρ_m and $N+1$ temporal points τ^n, defined by

$$\rho_0 = 1\,, \quad \rho_{m+1} = \rho_m + h_m\,, \quad \rho_{M+1} = \rho_{\max}\,,$$

$$\tau^0 = 0\,, \quad \tau^{n+1} = \tau^n + k^n\,, \quad \tau^N = \frac{t_l}{t_0}\,,$$

where the spatial and temporal step sizes are both positive. We will use constant $h_m = h$, while k^n is reduced during dissolution. We denote the hydrogen concentrations and relative bubble radii at these points in space and time by $c(\rho_m, \tau^n) = c_m^n$ and $\eta(\tau^n) = \eta^n$, respectively. Since the stretching factor $s(t)$ is dependent on time only, we also denote

$$s^n = \frac{\rho_{\max} - \eta^n}{\rho_{\max} - 1}$$

We approximate the derivatives in time by the (explicit) forward Euler method,

$$\partial_\tau c_m^n \approx \frac{c_m^{n+1} - c_m^n}{k^n}\,, \qquad \partial_\tau \eta^n \approx \frac{\eta^{n+1} - \eta^n}{k^n}\,.$$

The spatial derivatives are approximated using central differences,

$$\partial_\rho c_m^n \approx \frac{c_{m+1}^n - c_{m-1}^n}{2h}\,, \qquad \partial_\rho^2 c_m^n \approx \frac{c_{m+1}^n - 2c_m^n + c_{m-1}^n}{h^2}\,.$$

Discrete ODE

By inserting these discretizations into (3.14a) and defining

$$f^n = \frac{1}{\nu}\,\frac{Hc_g^n - c_0^n}{c_g^n - \frac{1}{3\eta^n}}\,, \tag{3.17}$$

the relative bubble radius at time τ^{n+1} is given by

$$\eta^{n+1} = \eta^n - k^n f^n\,, \tag{3.18}$$

and as such is only dependent on the bubble radius and boundary concentration at time τ^n.

Discrete PDE

The discrete version of (3.16a) is

$$\begin{aligned}\frac{c_m^{n+1} - c_m^n}{k^n} = &\frac{1}{s^n}\left(\left(\frac{\eta^n}{s^n\rho_m - (s^n-1)\rho_{\max}}\right)^2 - \frac{\rho_{\max}-\rho_m}{\rho_{\max}-1}\right) f_n \frac{c_{m+1}^n - c_{m-1}^n}{2h}\\ &+ \frac{1}{(s^n h)^2}\left(\frac{s^n h}{s^n\rho_m - (s^n-1)\rho_{\max}}(c_{m+1}^n - c_{m-1}^n) + c_{m-1}^n - 2c_m^n + c_{m+1}^n\right)\,,\end{aligned}$$

which can be rewritten to find the concentration at time τ^{n+1} in the form

$$c_m^{n+1} = A_m^n c_{m-1}^n + B_m^n c_m^n + C_m^n c_{m+1}^n\,. \tag{3.19}$$

The coefficients are:

$$\begin{aligned}A_m^n =& -\frac{k^n f^n}{2s^n h}\left(\left(\frac{\eta^n}{s^n\rho_m - (s^n-1)\rho_{\max}}\right)^2 - \frac{\rho_{\max}-\rho_m}{\rho_{\max}-1}\right)\\ &+ \frac{k^n}{(s^n h)^2}\left(1 - \frac{s^n h}{s^n\rho_m - (s^n-1)\rho_{\max}}\right)\end{aligned} \tag{3.20a}$$

$$B_m^n = 1 - \frac{2k^n}{(hs^n)^2} \tag{3.20b}$$

$$\begin{aligned}C_m^n =& \frac{k^n f^n}{2s^n h}\left(\left(\frac{\eta^n}{s^n\rho_m - (s^n-1)\rho_{\max}}\right)^2 - \frac{\rho_{\max}-\rho_m}{\rho_{\max}-1}\right)\\ &+ \frac{k^n}{(s^n h)^2}\left(1 + \frac{s^n h}{s^n\rho_m - (s^n-1)\rho_{\max}}\right)\end{aligned} \tag{3.20c}$$

Note that (3.19) only takes inputs of variables at time τ^n, and only holds for the interior points ($m = 1, 2, ..., M$). We can write this as a matrix equation:

$$\begin{pmatrix} c_1^{n+1} \\ \vdots \\ c_m^{n+1} \\ \vdots \\ c_M^{n+1} \end{pmatrix} = \begin{pmatrix} B_1^n & C_1^n & & & \\ & \ddots & & & \\ & A_m^n & B_m^n & C_m^n & \\ & & & \ddots & \\ & & & A_M^n & B_M^n \end{pmatrix} \cdot \begin{pmatrix} c_1^n \\ \vdots \\ c_m^n \\ \vdots \\ c_M^n \end{pmatrix} + \begin{pmatrix} A_1^n c_0^n \\ 0 \\ \vdots \\ 0 \\ C_M^n c_{M+1}^n \end{pmatrix} \tag{3.21a}$$

Or, equivalently,

$$\mathbf{C}^{n+1} = K^n \cdot \mathbf{C}^n + \mathbf{F}^n \,. \tag{3.21b}$$

Boundary conditions

Since (3.21) only holds for interior points of the domain, we need to consider how to implement the Boundary conditions. The boundary conditions are of Robin type both at $r_{\max}$ ($m = M + 1$) and at the interface ($m = 0$). Discretization of (3.16b) and (3.16c) gives

$$c_{M+1}^n + \frac{1}{s^n}\left(\frac{\rho_{\max}}{\eta^n}\right)^2 \frac{\partial_\rho c_{M+1}^n}{f^n} = 0 \tag{3.22a}$$

and

$$c_0^n - \frac{\nu}{s^n}\partial_\rho c_0^n = H c_g^n \,, \tag{3.22b}$$

respectively. The central difference approximation of the spatial derivatives at the end-points would require the knowledge of the concentration at ρ_{M+2} and ρ_{-1}. To avoid these points which lie outside our domain, the method of undetermined coefficients is employed to approximate the derivatives at these points by

$$\partial_\rho c_{M+1}^n = \frac{1}{2h}(3c_{M+1}^n - 4c_M^n + c_{M-1}^n) \,,$$

$$\partial_\rho c_0^n = \frac{1}{2h}(-3c_0^n + 4c_1^n - c_2^n) \,.$$

From (3.22) the discretized boundary conditions therefore become

$$c_{M+1}^n = \frac{4c_M^n - c_{M-1}^n}{2hs^n f^n \left(\frac{\eta^n}{\rho_{\max}}\right)^2 + 3} \,, \tag{3.23a}$$

$$c_0^n = \frac{4c_1^n - c_2^n + \frac{2hs^n}{\nu} H c_g^n}{\frac{2hs^n}{\nu} + 3} \,. \tag{3.23b}$$

In particular, we note that the concentration at the interface must be initialized so that

$$c_0^0 = \frac{H c_g^0}{1 + \frac{3\nu}{2h}} \,. \tag{3.24}$$

3.2.4 Computational algorithm

In order to find the lifetime t_l of a nanobubble with initial radius $\mathcal{R}_0$, i.e. the time it takes for complete dissolution, we use algorithm 3, where *tol* represents the relative bubble radius below which we consider the bubble dissolved. Note that for each time step we first calculate the new radius relative to the initial one (i.e. solve the ODE), before we build the necessary matrices to find the new concentration distribution at the interior points of our spatial domains. At the end of each time step, the Robin boundary conditions are updated.

```
Data: $\mathcal{R}_0$, $\alpha$, $\rho_{\max}$, $M$, $k^0$, $tol$
Result: $t_l$
$t_l = 0$;
initialize $\eta = 1$;
initialize $\mathbf{C} = 0$;
initialize $\mathbf{C}_0$ using (3.24);
while $\eta > tol$ do
    calculate new $\eta$ from (3.18);
    build $\mathbf{K}$ and $\mathbf{F}$ with (3.20);
    update $\mathbf{C}$ by solving (3.21);
    update $\mathbf{C}_0$ and $\mathbf{C}_{M+1}$ from (3.23);
    $t_l = t_l + t_0 k^n$;
    if $k^n$ is too small/large then
        increase/decrease $k^n$;
    end
end
```

Algorithm 3: Dissolution time for nanobubble

3.2.5 System parameters

The system parameters shown in table 3.2 have been used except where specified otherwise. A larger value for $\rho_{\max}$ gives a better implementation of our condition that the hydrogen concentration is zero "far from the bubble", and combined with the amount of interior nodal points M, it sets the spatial resolution h of our numerical procedure. We expect the concentration changes to occur mainly near the bubble surface. Hence, a domain ten times longer than the initial radius of the bubble is selected. We choose k^0 small enough to ensure that the temporal steps are not too large, and we update k^n if it is so small that the runtime becomes excessively large.

Table 3.2: Default parameters used in numerical model for computing nanobubble lifetime.

$\rho_{\max}$ $[-]$	M $[-]$	k^0 $[-]$	tol $[-]$
10	100	10^{-5}	10^{-3}

3.3 Computational specifications

The computer which has been used for simulations is a Dell Optiplex 980 with an Intel Core i7 860 CPU @ 2.80GHz × 4 and 16 GB RAM running Ubuntu 14.04 LTS.

Chapter 4

Results

4.1 Steady-state surface nanobubble

The results in this section come from FEM simulations in the model for the steady-state surface nanobubble. We present qualitative results showing the concentration distribution in the domain along with contour lines and vector flow diagrams to illustrate the system behaviour. These results are obtained from the 2D model. We also use results from the 2D model to show how the error behaves when we implement algorithm 1. Plots of molar flux J_0 of hydrogen at the electrode surface versus the mass transfer coefficient α are given from both the 2D and 3D model.

4.1.1 Concentration distribution

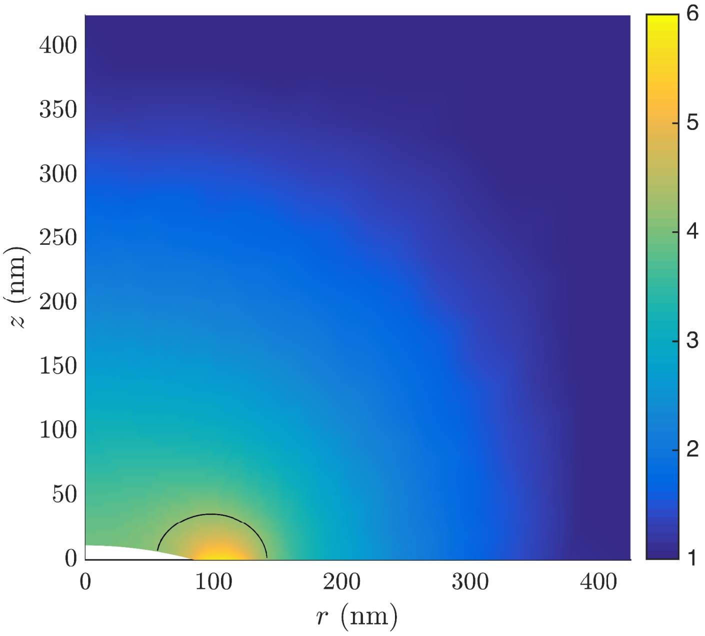

Figure 4.1: Hydrogen concentration distribution C_l/C_{sat} at dynamic equilibrium for a 80 nm surface nanobubble in the 2D model with $\alpha = 0.1\,\text{m/s}$. The black line shows the contour line $C_l = HC_g$.

In figure 4.1 the relative concentration of hydrogen in the different parts of the domain is shown as a surface plot with typical parameters for the model. To illustrate how the flow of hydrogen behaves near the bubble, we have drawn contour plots and vector fields for different values of α in figure 4.2.

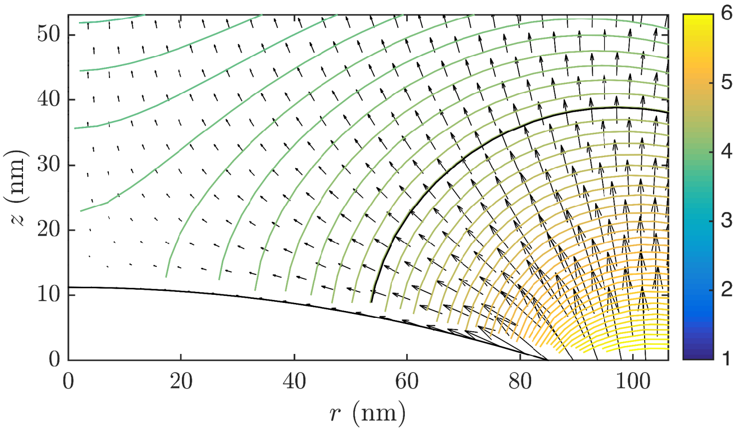

(a) $\alpha = 10^{-3}\,\mathrm{m/s}$

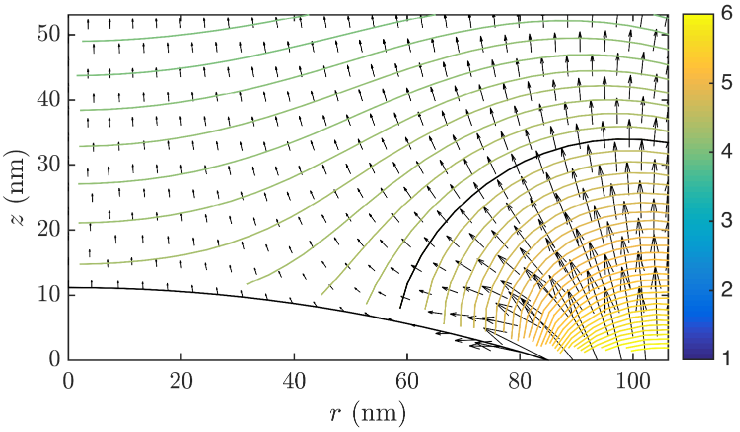

(b) $\alpha = 0.2\,\mathrm{m/s}$

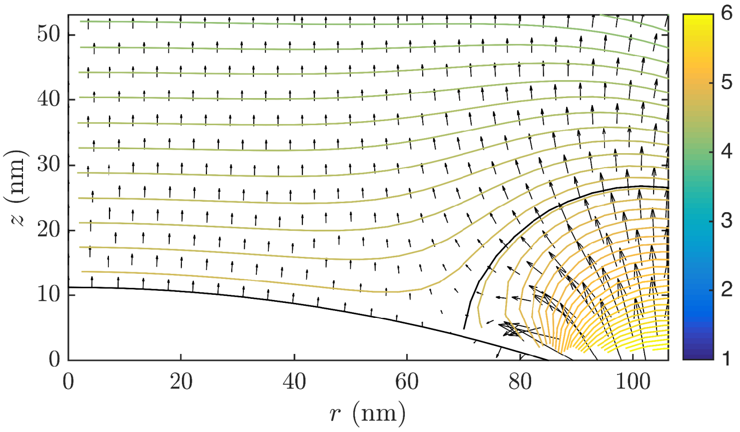

(c) $\alpha = 10\,\mathrm{m/s}$

Figure 4.2: Gradients and vector fields near the bubble interface of a 80 nanometer surface nanobubble for different values of α. Also in these plots the black line indicates the contour line $C_l = HC_g$.

4.1.2 Error behaviour

Figure 4.3 shows stem plots of the relative error ε and how it is altered for each iteration. Note that the plot in figure 4.3a shows a poor initial choice for the flux and thus a correspondingly large error, while the others start at smaller errors. Since the tolerance is so small, however, this initial guess is not too important, and the amount of iterations it takes to reduce the error to a small enough value is much more dependent on finding a proper proportionality coefficient. For all cases, the relative error approaches zero after maximum 20 iterations.

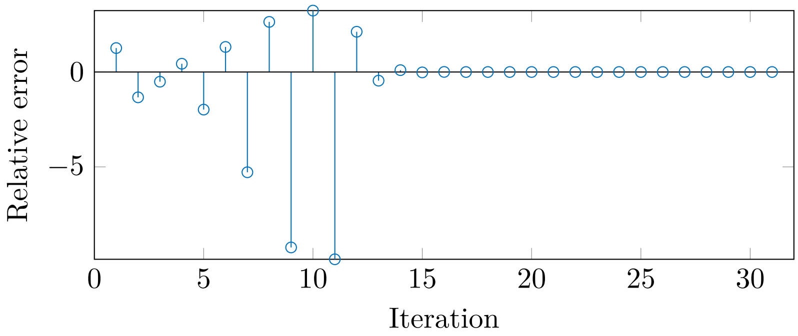

(a) $\alpha = 10^{-3}\,\mathrm{m/s}$

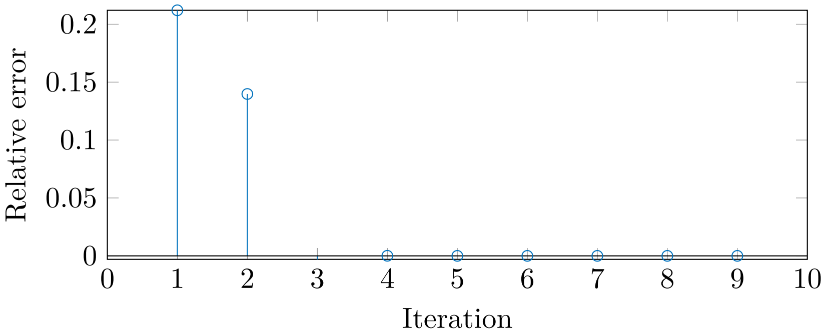

(b) $\alpha = 0.2\,\mathrm{m/s}$

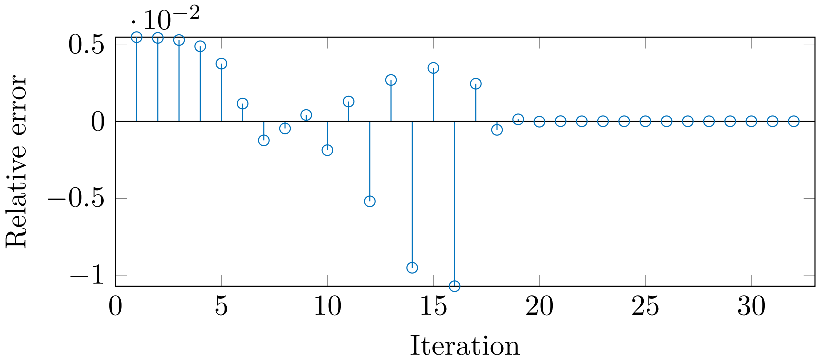

(c) $\alpha = 10\,\mathrm{m/s}$

Figure 4.3: Illustration of how the relative error behaves per iteration and how many iterations are needed to reach tolerable values. Note that figures (a) and (c) show typical worst-case scenarios. When solving for many values of α consecutively, the average number of iterations per case is around 10.

4.1.3 Dependency of molar flux on mass transfer coefficient

Since we are interested in how the supplied current required to sustain dynamic equilibrium for a surface nanobubble depends on the mass transfer coefficient of the bubble surface, we make log-log plots of J_0 as a function of α. Figure 4.4 shows the behaviour for a nanobubble with contact radius $r_b = 85$ nm for both the 2D and the 3D model, while figure 4.5 includes several different bubble sizes.

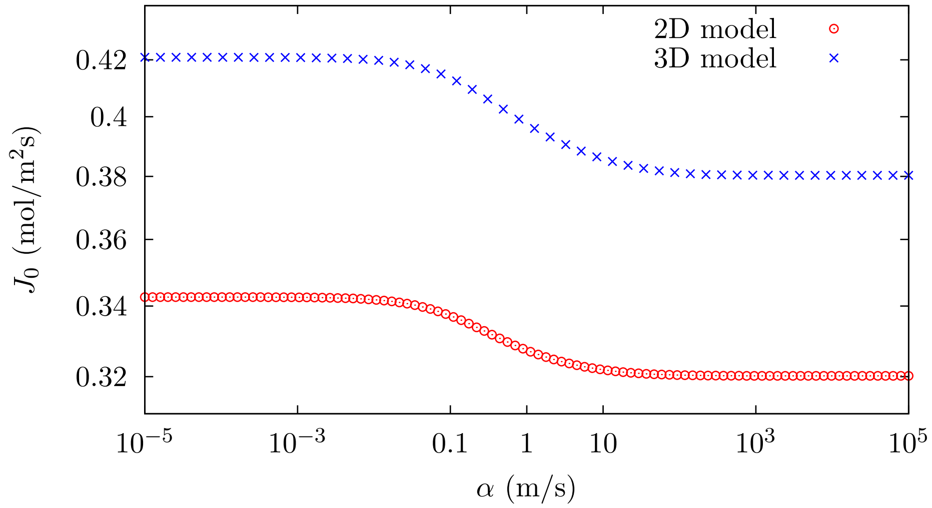

Figure 4.4: Equilibrium current J_0 required to sustain a nanobubbles with surface radius $r_b = 85\,\text{nm}$ as a function of the mass transfer coefficient α. The results from the 2D and 3D model have 50 and 100 points with logarithmically increasing spacing, respectively.

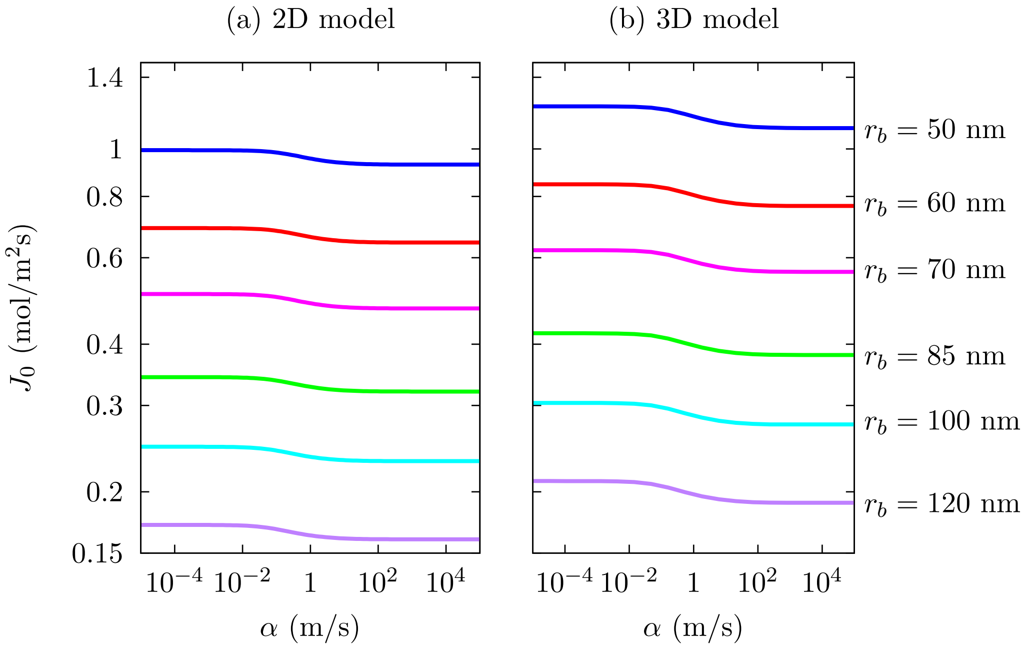

Figure 4.5: Equilibrium current J_0 as a function of α for various nanobubble sizes.

4.2 Dissolution of bulk nanobubble

It is the goal of the model for the dissolving bulk nanobubble to shed some light on the actual lifetime of such bubbles. We present results which reveal both how the bubble size changes with time and how this behaviour depends on the initial radius $\mathcal{R}_0$ of the bubble as well as the value of the mass transfer coefficient α. We also test the model behaviour by investigating the conservation of hydrogen molecules in the liquid.

4.2.1 Lifetime of bulk nanobubble

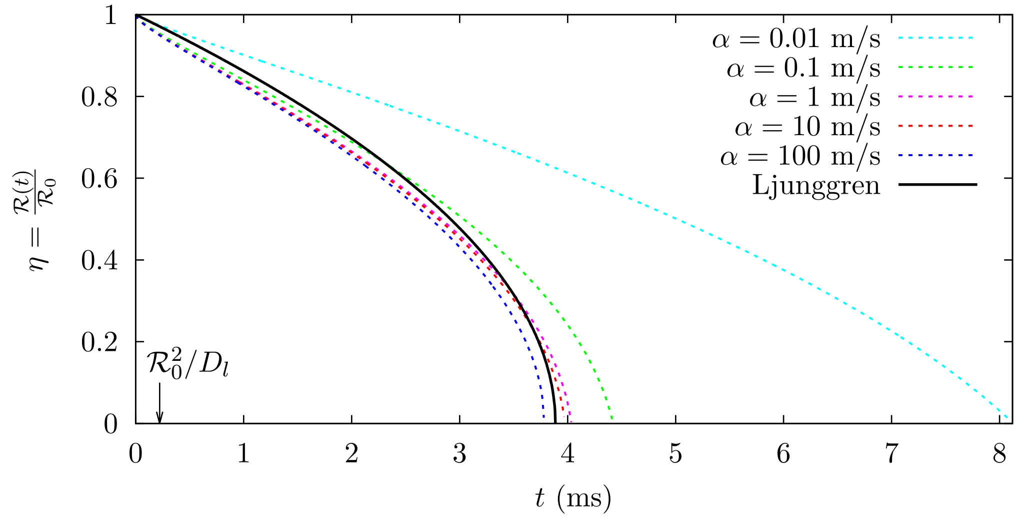

(a) $\mathcal{R}_0 = 10^{-6}$ m

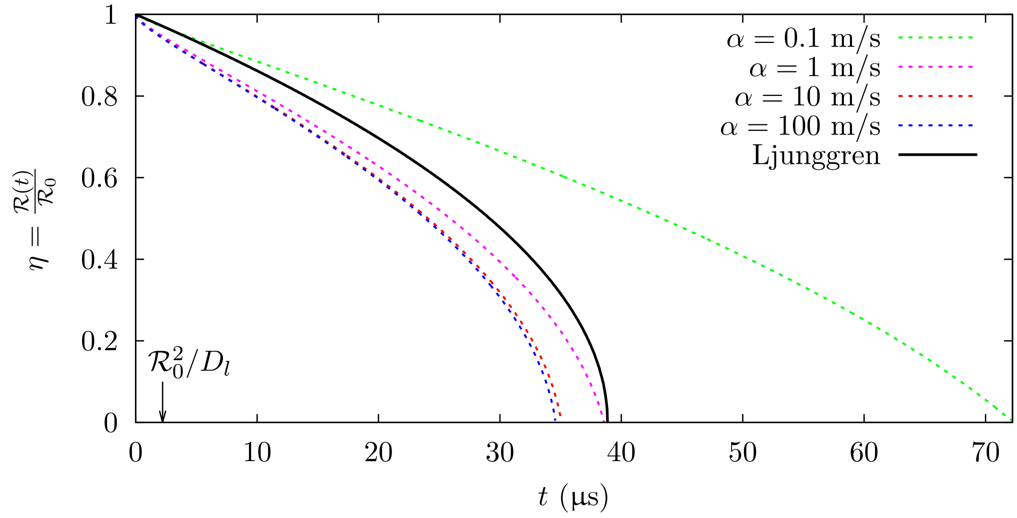

(b) $\mathcal{R}_0 = 10^{-7}$ m

Figure 4.6: Relative bubble radius η as a function of time for a bulk nanobubble with initial radius of (a) 10^{-6} m and (b) 10^{-7} m and various values for the mass transfer coefficient α. The expected behaviour according to (2.38) in the analytical model by Ljunggren et al. is included for comparison, and the lifetime quoted for surface nanobubbles in most literature[10,13,17,20,21] on the subject is indicated on the time axis.

Figure 4.6 shows how the radius of the nanobubble shrinks as the dissolution takes place for two different initial bubble radii, and comparisons with literature are included. In order to get an idea of how the lifetime depends on $\mathcal{R}_0$ and α, the plots in figure 4.7 are presented. The same data is plotted with logarithmically scaled axes in figure 4.8 to check how our model compares with the $\mathcal{R}_0^2$-dependency presented in the literature.

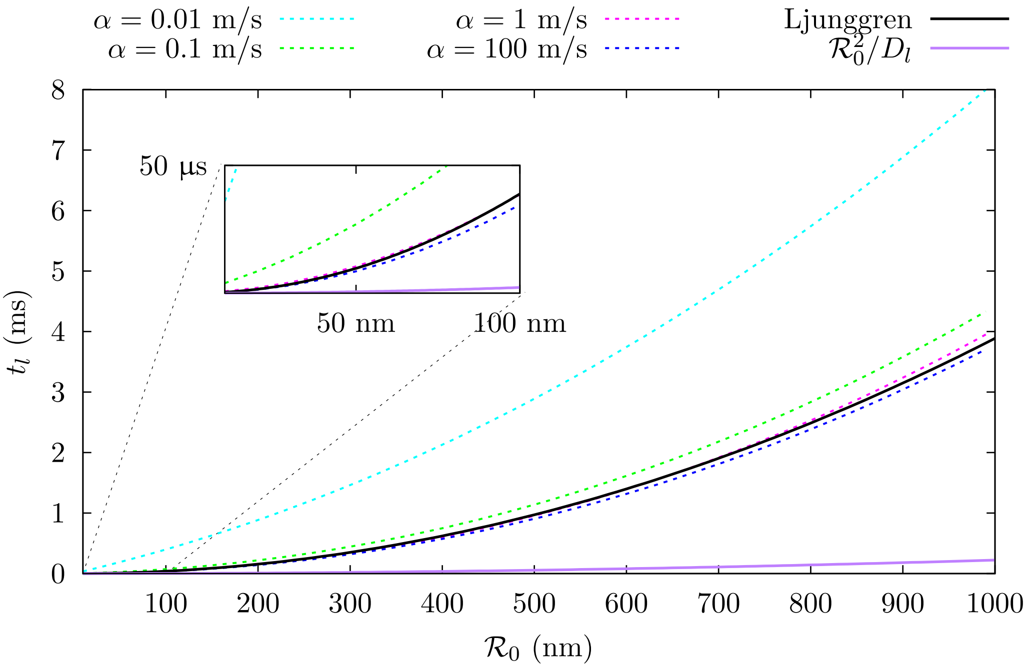

Figure 4.7: Lifetime t_l required for complete dissolution for bulk nanobubbles with initial radius $\mathcal{R}_0$ varying between 10 nm and 1 µm. Inset: magnification for small initial radii.

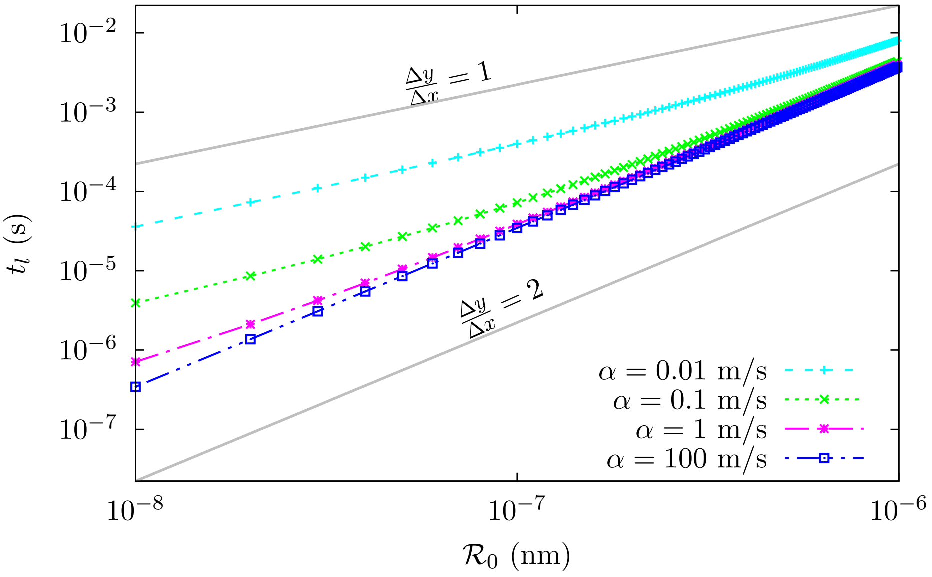

Figure 4.8: Lifetime t_l plotted against initial radius $\mathcal{R}_0$ with logarithmic scaling on both axes for various α. The upper and lower dashed black lines illustrate a slope equal to 1 and 2, respectively.

4.2.2 Conservation of hydrogen

As a test of how our numerical model performs, we have calculated the relative number of hydrogen molecules in the gas and liquid phases as a function of time, in addition to the total amount. To find the amount of H_2 molecules in the gas, we multiplied the nanobubble volume at a given time with the gas concentration, while the liquid molecule amount was found by numerical integration using the trapezoidal rule for all data points in the liquid. The total amount of hydrogen molecules in the system should in theory be conserved, as described in appendix B. From a typical plot of relative amount of hydrogen molecules, like that shown in figure 4.9, we see that this criterion is nearly fulfilled, although a slight increase of approximately 5% is observed during the time required for dissolution.

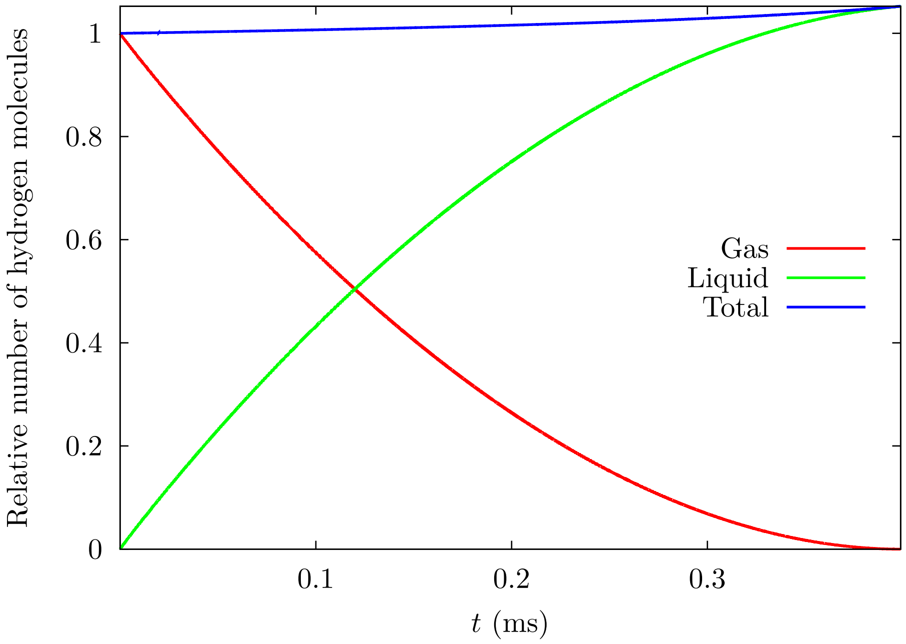

Figure 4.9: Relative number of hydrogen molecules in the system. The amount of H_2 molecules in the gas and liquid phases are shown individually, along with the sum of the two. The system parameters used to generate this plot were $\mathcal{R}_0 = 10^{-7}$ m and $\alpha = 0.01$ m/s.

Chapter 5

Discussion

5.1 Validity of dynamic-equilibrium model

5.1.1 System behaviour

The concentration distribution in figure 4.1 shows a qualitative result that we would expect. To understand where the different regions of the domain are, the reader is encouraged to compare with figure 3.2. Far from the bubble, at the Dirichlet boundary, we demand $C_l = C_{\text{sat}}$, which we immediately see is fulfilled by noting the corresponding colours on the bar in the right of the figure. The high concentration to the immediate right of the three-phase point is due to the electrolysis occurring on the free electrode surface. It is the molar flux per area across this surface, J_0, which we iterate to find the correct value of. From this surface the supplied hydrogen gas propagates through the domain, and we therefore see a steady decline in the hydrogen concentration as we move away from it. At the zero-flux boundaries (above the bubble apex and along the glass to the right of the electrode) we expect the concentration gradient to be parallel with the boundary, and it certainly looks that way. Lastly, we note that the curved black line enclosing the free electrode surface, which is a $C_l = HC_g$ contour line, intersects with the surface nanobubble. This is a necessity for our dynamic equilibrium to make sense since it means that we have a flux of hydrogen into and out of the bubble on the parts of the nanobubble surface that lie inside and outside of the contour line, respectively.

By studying the contour plots and vector fields in figure 4.2, we obtain a more detailed understanding of the hydrogen flow. On a contour line the concentration in the liquid is constant, so its gradient is always perpendicular to these lines. In all of the plots we see clearly that there is no net flux across the zero-flux boundary above the bubble apex since all flow is vertical and away from the bubble. The difference between the three subfigures is the value of the mass transfer coefficient α, which is greatly increased from each plot to the next. Recall that α is the proportionality factor which relates the flux through the surface to the concentration difference across it according to (2.29). In figure

4.2a, where we have $\alpha = 10^{-3}$ m/s, we see that the flow of hydrogen is along the bubble surface, corresponding to practically zero flux across the boundary. This is as expected - setting a small enough value for α in the Robin condition (3.1d) just gives us a zero-flux Neumann condition. For the second plot, we have set $\alpha = 0.2$ m/s, leading to an interesting case where a significant part of the hydrogen produced through electrolysis enters the nanobubble in the region where $Cl > HC_g$ and leaves it where $Cl < HC_g$. Note that the vectors pointing into the nanobubble are longer than those pointing out of it, meaning that the flow described by them is larger. This is the reason why a larger part of the bubble surface is in contact with liquid having $C_l < HC_g$, since the total flux through the surface must cancel out according to (2.5). In the last case, we have a large α with a value of 10 m/s. Here, the flow through the bubble surface is normal to the surface over the entire boundary, and the vectors are generally very small. The concentration is very close to $C_l = HC_g$ along the entire boundary, which makes sense since the limiting case of (3.1d) for large α corresponds to a Dirichlet condition where $C_l = HC_g$. As α is increased from (a) to (c), we see that the area where $C_l > HC_g$ shrinks, and that the contour lines outside of this area grow more uniform. If the dynamic-equilibrium effect is in fact a significant contribution to the stability of surface nanobubbles, we expect a scenario closest to that depicted in figure 4.2b.

5.1.2 Equilibrium flux as a function of mass transfer coefficient

As is clearly shown in figure 4.4, the necessary supplied current required to sustain a nanobubble of a given size and geometry depends very weakly on what value we choose for the mass transfer coefficient. As α is increased from 10^{-5} m/s to 10^{-2} m/s the equilibrium current is practically constant. A very slight decrease (less than 10%) occurs as we move from 0.01 m/s to 10 m/s, after which it again remains constant as α is increased to 10^5 m/s. In figure 4.5, the same numerical experiments have been performed with various sizes of the surface nanobubble, and they all show similar results. As the size of the nanobubble is increased, the required production of hydrogen per unit area decreases, but it is important to remember that since we have $r_d = 1.5r_b$, the area of the free electrode surface grows proportionally to r_b^2. The slight shift that we see when moving from two to three dimensions is not surprising as the 2D model has obvious limitations in accuracy and also conceptually. The fact that only a very small range of values for the equilibrium molar flux allows the surface nanobubble of a given size to be kept at dynamic equilibrium regardless of the mass transfer coefficient, is a very important point. It means that if we had a surface nanobubble of a different size than that corresponding to its equilibrium flux, the nanobubble would adapt and change its size accordingly. This underlines a crucial dependency of the nanobubble size (here represented by r_b) on the equilibrium current that supports the ideas behind the dynamic-equilibrium model.

5.2 Lifetime of bulk nanobubble

5.2.1 Bubble behaviour and its dependencies

Our numerical model for the dissolution of the bulk nanobubble shows some very interesting results. Figure 4.6 exhibits how the bubble shrinks as time passes, given two different initial bubble radii, namely (a) $\mathcal{R}_0 = 10^{-6}\,\mathrm{m}$ and (b) $\mathcal{R}_0 = 10^{-7}\,\mathrm{m}$. The dashed coloured lines show results from our numerical model, each corresponding to a specific value of α. Note that the intersection of a curve with the primary axis denotes the lifetime for a nanobubble with corresponding parameters. It is evident that smaller α lead to more rapid dissolution and hence shorter lifetimes, while for small α the lifetime drastically increases. The dependency of t_l on α follows intuitively since a higher α means that more hydrogen is transmitted through the bubble surface for a given concentration difference, leading to quicker dissolution of the bubble. According to (2.38) in the analytical model by Ljunggren et al.[36], the bubble radius should behave as shown by the solid black line in the plots. This corresponds very well with our model as long as α is large enough. For small α, we predict a far longer lifetime. This difference becomes increasingly important for smaller initial bubble sizes, demonstrated by how the green line behaves in subplot (a) compared to in (b). Lastly, we note that the quoted lifetime from most nanobubble literature, $t_l = \mathcal{R}_0^2/D_l$, is approximately 20 times shorter than all other results. When also taking into consideration the other arguments we have presented to show that surface nanobubbles should have much longer lifetimes than those in bulk, and that our model computes a lower bound on the lifetime, it is evident that this literature value does not apply at all to the actual circumstances.

As seen from figure 4.7, the lifetime of a bulk nanobubble decreases rapidly with its initial radius. Again, we see how much smaller the lifetimes are in the simplistic $\mathcal{R}_0^2/D_l$ model compared to the numerical results and those proposed by Ljunggren et al., and note that for small α our numerical model yields much longer lifetimes than even that of Ljunggren et al. Interestingly, we see that for bubbles with $\mathcal{R}_0 < 100$ nm, the differences between our small-α computations and the Ljunggren remain larger than for larger bubbles, suggesting a dependency on $\mathcal{R}_0$ which differs from the square-law presented by both analytical expressions. Figure 4.8 allows us to investigate this behaviour further. Since the axes are scaled logarithmically, we would expect the lifetime to have a slope equal to 2 for a square-law dependency. When comparing our results with such a slope (the grey line marked $\Delta y/\Delta x = 2$) we see that we indeed find parallel lines for larger α. For small α, this only holds for the largest values for $\mathcal{R}_0$, and for small bubbles the results are surprisingly more aligned with a slope equal to 1, hinting at a linear dependency on $\mathcal{R}_0$! Since there is a smooth transition from one slope to the other, we observe a dependency on $\mathcal{R}_0$ which is not described by a power-law. This is not surprising, since we are not making the same simplifications as the other models. This could mean that the lifetime for sufficiently small bubbles is in fact described by some function which approaches zero a lot slower than $\mathcal{R}_0^2$. This could therefore be an important point in explaining the longevity of nanobubbles.

5.2.2 Increase in hydrogen amount

There is a slight increase in the amount of hydrogen molecules, as shown in figure 4.9. Let us first describe what the plot shows. At the initial time all hydrogen molecules are inside the bubble. As we proceed forward in time, they dissolve through the surface and into the liquid, until no molecules remain in the gas state when the bubble is completely dissolved. The number of molecules in the liquid state grows accordingly, so that when the bubble is completely dissolved, all of the hydrogen molecules are in the liquid phase. Our problem is that the amount of hydrogen molecules in the liquid end up at a slightly higher amount than what was initially in the nanobubble. This is also reflected in the total hydrogen amount, plotted as a blue line, which should stay constant at 100% at all times.

Altering system variables like $\mathcal{R}_0$, α and D_l alter the behaviour of the system as a whole, but this has no direct effect on the particle amount as a function of time. This suggests that the problem lies either in our model or in the numerical implementation. Since the derivation of our model includes tedious mathematical manipulations, there is room for error in, for example, the transformation of our PDE from the actual time-dependent domain to the time-independent reference domain.

Since finite-difference schemes are identical to finite-volume schemes in one dimension, conservation of mass and particle amount is expected to hold. One probable cause of error in the numerics is the implementation of an explicit Euler method for the temporal discretization. In order for this scheme to give a reasonable approximation of the actual system behaviour, we need the Courant-Friedrichs-Lewy condition to be satisfied. For a PDE with parabolic behaviour, which we have if the diffusive term is dominant, the condition is

$$k^n \leq Ch^2 \,,$$

where C is some constant which depends on the diffusion coefficient as $C \propto 1/D_l$. A straightforward way to avoid this condition is to implement an implicit scheme for the temporal discretization but due to the coupling of the ODE and PDE this is no trivial task.

Chapter 6

Proposed further work

6.1 Solve problem with conservation of hydrogen

The lack of hydrogen conservation as shown in figure 4.9 is a concern with our model. Although the increase in the amount of molecules is only around 5%, the effect on the system cannot be proven to be negligible. A first attempt to solve this discrepancy would be the implementation of an implicit scheme instead of the explicit one used currently. This would omit the possibility that the temporal step size is too large. The difference between an explicit and an implicit scheme is that implicit schemes require the solution of an equation that includes the state of the system both at the current time and at a later time. Simply put, if $y(t)$ is the state of a system at time t, explicit methods give the state at a later time as

$$y(t + \Delta t) = f(y(t))\,, \tag{6.1}$$

while an implicit scheme requires solving an equation of the form

$$g(y(t), y(t + \Delta t)) = 0\,. \tag{6.2}$$

If the problem persists after an implicit scheme has been implemented, and further efforts to find mistakes in the mathematics for the domain transformation prove fruitless, the original governing equations should be revisited.

6.2 Consider system of many bubbles

With the exception of Luo and White's experiment [8], all experimental results on nanobubbles stem from experiments where nanobubbles are generated in large numbers. Although the model of a single nanobubble is extremely elegant and easy to duplicate numerically, little of the supporting evidence and measured properties of nanobubbles are derived from this model. It would therefore be very interesting to see what results we obtain for the surface nanobubble if we simulate an array of hydrogen bubbles, reflected by periodic boundary conditions. This would correspond to zero-flux conditions at all sides, flux due to electrolysis at the substrate surface not covered by the nanobubble, and a constant concentration at some vertical distance over the nanobubble. A mesh shaped like a rectangular box would give easy implementation of the boundary conditions. If the model was extended to include possibilities for multiple bubble analysis, phenomena such as bubble interaction could be considered.

6.3 Combine our two approaches

In one model, we have simulated the behaviour of a steady-state surface nanobubble in an advanced 3D simulation based on FEM and in another model the dynamic behaviour of a bulk nanobubble using a time-dependent domain and FDM was simulated. The thought of combining these two in a single model to simulate a dynamic surface bubble, which is allowed to grow or shrink according to the system's molar influx J_0, would be a truly intriguing (yet computationally challenging) endeavour.

6.4 Investigate connection to electrochemical kinetics

Of particular importance is the Butler-Volmer equation, which describes the relationship between the applied potential on an electrode and the resulting electrical current,

$$I = A_a \cdot J_{\mathrm{ex}} \left(\exp\left(\frac{\alpha_a n_e F \Delta E}{RT}\right) - \exp\left(\frac{\alpha_c n_e F \Delta E}{RT}\right)\right) . \tag{6.3}$$

I is the current, A_a the active electrode surface area, J_{ex} the exchange current density of the electrode, n_e the amount of electrodes in the reaction, ΔE the difference of the electrode potential from its equilibrium value and α_a and α_c the charge transfer coefficients for the anode and cathode, respectively. Since the papers concerning formation of surface nanobubbles due to electrolysis exhibit relationships between bubble nucleation and applied voltage, numerical experiments seeking to quantify these relationships could give further insight into nanobubble behaviour.

6.5 Derive thorough irreversible thermodynamics

In subsection 2.2.1, we made the step from (2.15) to (2.16) with only a few comments, employing simplifications present throughout this thesis. It would be interesting to derive flux equations without making as many simplifications, since it has been shown time and time again that ”paradoxes” (as the superstability of nanobubbles has been called) are often simply experimental anomalies that cannot be explained within theories derived from simplifying assumptions. Of biggest interest would be the inclusion of the electric potential term, but the transport of water and Gibb's reaction energies could also affect the system more than expected.

6.6 Improve accuracy of numerical methods, use HPC

Apart from the implementation of an implicit scheme to avoid the condition on k^n, our implementations of both FDM and FEM could be improved by making finer spatial meshes and, for FDM, reducing the temporal step size. This would, however, increase the computational cost and to avoid excessive runtimes, a natural step would be to investigate whether the scripts can be altered to enable parallel processing. The systems could be solved on more powerful computers, taking advantage of high performance computing (HPC).

Since the accuracy of FEM increases both with the node amount N and with the polynomial degree of the test functions on each element, we could further improve the FEM procedure by using e.g. quadratic basis functions in the finite elements. The calculations would lead to longer computational times for quadratic elements than linear ones but fewer nodes would be needed to reach the same accuracy. To optimize the numerical procedure, the cost/gain in using quadratic elements instead of linear ones should be investigated. With reference to (C.9), the numerical solution u_h could be sought in the function space

$$X_h^2 = \{v \in H^1_{\partial\Omega_D} : v|_{K_k} \in \mathbb{P}_2(K_k), 1 \leq k \leq M\}\,. \tag{6.4}$$

A similar improvement of the FDM scheme would be to include contributions from more neighbours when using the method of undetermined coefficients. Instead of considering contributions from the two nearest neighbours only on the interior of the domain, we could for example use four nearest neighbours.

Chapter 7

Conclusion

We have developed two numerical models which seek different approaches to investigating the dynamic-equilibrium model proposed to explain superstability of surface nanobubbles. The two models have in common that the flux through the nanobubble surface is modelled by a combination of Henry's law and a Taylor expansion around the equilibrium concentrations in the interior and exterior of the bubble. They thus take into consideration that the bubble is not in chemical equilibrium. They also both consider nanobubbles of ideal hydrogen in water at room temperature and atmospheric pressure.

The first model concerns a surface nanobubble of fixed size due to constant hydrogen production from electrolysis at the platinum electrode to which it is connected. By defining the nanobubble size and geometry, in addition to the mass transfer coefficient α for the gas/liquid surface, the steady-state solution where the condition for dynamic equilibrium is satisfied is determined. This is done by solving the Laplace equation in the liquid domain and varying the molar flux J_0 from electrolysis. The numerical scheme is a finite-element procedure on a non-trivial three-dimensional domain with a mix of Dirichlet, Neumann and Robin conditions. The model works well and shows results as expected, and there is a relationship between J_0, α and the nanobubble size which suggests that for a given applied current there is a suitable bubble geometry which can be balanced by the dynamic equilibrium mechanism.

Our second model was motivated by vague and simplistic arguments surrounding the "paradox" in nanobubble literature. In order to obtain a better approximation of the lifetimes of bulk nanobubbles, which yield lower limits for the longevity than those on surfaces, we have coupled the scalar transport equation on the time-dependent domain outside the bubble with an ODE for the bubble radius derived from mass conservation at the interface. We solved the system of equations numerically by transforming them to a reference domain, and by implementing spatial finite-difference discretizations and a temporal forward Euler scheme. Our results look promising when compared to analytical models and give lifetimes an order of magnitude higher than those quoted in the literature, although we observe a slight discrepancy in the conservation of hydrogen molecules in our system.

Bibliography

[1] Knut Sverdrup Kleppestø. Numerical simulation of the dynamical equilibrium model for nanobubble stability. Specialization project report, 2014.

[2] Asbjørn H. Sperre. Modelling surface nanobubbles in water electrolysis. Master's thesis, Norwegian University of Science and Technology, 2015.

[3] John L. Parker, Per M. Claesson, and Phil Attard. Bubbles, cavities, and the long-ranged attraction between hydrophobic surfaces. *Journal of Physical Chemistry*, 98(34):8468–8480, 1994.

[4] Shi-Tao Lou, Zhen-Qian Ouyang, Yi Zhang, Xiao-Jun Li, Jun Hu, Min-Qian Li, and Fu-Jia Yang. Nanobubbles on solid surface imaged by atomic force microscopy. *Journal of Vacuum Science & Technology B*, 18(5):2573–2575, 2000.

[5] Naoyuki Ishida, Taichi Inoue, Minoru Miyahara, and Ko Higashitani. Nano bubbles on a hydrophobic surface in water observed by tapping-mode atomic force microscopy. *Langmuir*, 16(16):6377–6380, 2000.

[6] Shangjiong Yang, Peichun Tsai, E. S. Kooij, Andrea Prosperetti, Harold J. W. Zandvliet, and Detlef Lohse. Electrolytically generated nanobubbles on highly orientated pyrolytic graphite surfaces. *Langmuir*, 25(3):1466–1474, 2009.

[7] Lijuan Zhang, Yi Zhang, Xuehua Zhang, Zhaoxia Li, Guangxia Shen, Ming Ye, Chunhai Fan, Haiping Fang, and Jun Hu. Electrochemically controlled formation and growth of hydrogen nanobubbles. *Langmuir*, 22(19):8109–8113, 2006.

[8] Long Luo and Henry S. White. Electrogeneration of single nanobubbles at sub-50-nm-radius platinum nanodisk electrodes. *Langmuir*, 29(35):11169–11175, 2013.

[9] Maria Holmberg, Anders Kühle, Jørgen Garnæs, Knud A. Mørch, and Anja Boisen. Nanobubble trouble on gold surfaces. *Langmuir*, 19(25):10510–10513, 2003.

[10] James R. T. Seddon, Harold J. W. Zandvliet, and Detlef Lohse. Knudsen gas provides nanobubble stability. *Physical Review Letters*, 107(11):116101, 2011.

[11] Xue Hua Zhang. Quartz crystal microbalance study of the interfacial nanobubbles. *Physical Chemistry Chemical Physics*, 10:6842–6848, 2008.

[12] Hyejung Seo, Myungsun Yoo, and Sangmin Jeon. Influence of nanobubbles on the adsorption of nanoparticles. *Langmuir*, 23(4):1623–1625, 2007. PMID: 17243739.

[13] Xue H. Zhang, Abbas Khan, and William A. Ducker. A nanoscale gas state. *Physical Review Letters*, 98(13):136101, 2007.

[14] M. Switkes and J. W. Ruberti. Rapid cryofixation/freeze fracture for the study of nanobubbles at solid–liquid interfaces. *Applied Physics Letters*, 84(23):4759–4761, 2004.

[15] Henri Lhuissier, Detlef Lohse, and Xuehua Zhang. Spatial organization of surface nanobubbles and its implications in their formation process. *Soft Matter*, 10(7):942–946, 2014.

[16] James R. T. Seddon, Detlef Lohse, William A. Ducker, and Vincent S. J. Craig. A deliberation on nanobubbles at surfaces and in bulk. *ChemPhysChem*, 13(8):2179–2187, 2012.

[17] Michael P. Brenner and Detlef Lohse. Dynamic equilibrium mechanism for surface nanobubble stabilization. *Physical Review Letters*, 101:214505, Nov 2008.

[18] Xue Hua Zhang, Anthony Quinn, and William A. Ducker. Nanobubbles at the interface between water and a hydrophobic solid. *Langmuir*, 24(9):4756–4764, 2008.

[19] William A. Ducker. Contact angle and stability of interfacial nanobubbles. *Langmuir*, 25(16):8907–8910, 2009. PMID: 19624143.

[20] Siddhartha Das. Effect of impurities in the description of surface nanobubbles: Role of nonidealities in the surface layer. *Physical Review E*, 83:066315, Jun 2011.

[21] Nikolai D. Petsev, M. Scott Shell, and L. Gary Leal. Dynamic equilibrium explanation for nanobubbles' unusual temperature and saturation dependence. *Physical Review E*, 88:010402, Jul 2013.

[22] Joost H. Weijs and Detlef Lohse. Why surface nanobubbles live for hours. *Physical Review Letters*, 110(5):054501, 2013.

[23] W. Steckelmacher. Knudsen flow 75 years on: the current state of the art for flow of rarefied gases in tubes and systems. *Reports on Progress in Physics*, 49(10):1083, 1986.

[24] Zhihua Wu, Xuehua Zhang, Xiaodong Zhang, Gang Li, Jielin Sun, Yi Zhang, Minqian Li, and Jun Hu. Nanobubbles influence on bsa adsorption on mica surface. *Surface and Interface Analysis*, 38(6):990–995, 2006.

[25] Zhihua Wu, Hongbing Chen, Yaming Dong, Huiling Mao, Jielin Sun, Shenfu Chen, Vincent S.J. Craig, and Jun Hu. Cleaning using nanobubbles: Defouling by electrochemical generation of bubbles. *Journal of Colloid and Interface Science*, 328(1):10 – 14, 2008.

[26] Guangming Liu, Zhihua Wu, and Vincent S. J. Craig. Cleaning of protein-coated surfaces using nanobubbles: An investigation using a quartz crystal microbalance. *Journal of Physical Chemistry C*, 112(43):16748–16753, 2008.

[27] Hongbing Chen, Huiling Mao, Liping Wu, Jun Zhang, Yaming Dong, Zhihua Wu, and Jun Hu. Defouling and cleaning using nanobubbles on stainless steel. *Biofouling*, 25(4):353–357, 2009.

[28] Shangjiong Yang and Anton Duisterwinkel. Removal of nanoparticles from plain and patterned surfaces using nanobubbles. *Langmuir*, 27(18):11430–11435, 2011.

[29] Yuliang Wang, Bharat Bhushan, and Xuezeng Zhao. Improved nanobubble immobility induced by surface structures on hydrophobic surfaces. *Langmuir*, 25(16):9328–9336, 2009.

[30] Yuliang Wang and Bharat Bhushan. Boundary slip and nanobubble study in micro/nanofluidics using atomic force microscopy. *Soft Matter*, 6(1):29–66, 2010.

[31] Marie-Charlotte Audry, Agnès Piednoir, Pierre Joseph, and Elisabeth Charlaix. Amplification of electro-osmotic flows by wall slippage: direct measurements on ots-surfaces. *Faraday Discussions*, 146:113–124, 2010.

[32] S. Kjelstrup, D. Bedeaux, and E. Johanness. *Elements of Irreversible Thermodynamics for Engineers.* Akademika Publishing, 2006.

[33] J. G. Wijmans and R. W. Baker. The solution-diffusion model: a review. *Journal of Membrane Science*, 107(1):1–21, 1995.

[34] R. Sander. Compilation of Henry's law constants (version 4.0) for water as solvent. *Atmospheric Chemistry and Physics*, 15(8):4399–4981, 2015.

[35] P. S. Epstein and M. S. Plesset. On the stability of gas bubbles in liquid-gas solutions. *Journal of Chemical Physics*, 18(11):1505–1509, 1950.

[36] Stig Ljunggren and Jan Christer Eriksson. The lifetime of a colloid-sized gas bubble in water and the cause of the hydrophobic attraction. *Colloids and Surfaces A: Physiochemical and Engineering Aspects*, 129:151–155, 1997.

[37] Sven-Joachim Kimmerle. Modelling, simulation and stability of free surface and bulk nanobubbles in hydrogen electrolysis. In *Mathematical Modelling*, volume 8, pages 621–626, 2015.

[38] Alfio Quarteroni. *Numerical Models for Differential Problems.* MS&A. Springer, 2010.

[39] Per-Olof Persson and Gilbert Strang. A simple mesh generator in matlab. *SIAM Review*, 46(2):329–345, 2004.

[40] Christopher E. Brennen. *Cavitation and Bubble Dynamics.* Cambridge University Press, 2013.

Appendix A

The Laplace transform

For a real function $f(t)$ defined for $t \geq 0$, the (unilateral) Laplace transform is

$$\bar{f}(p) = \mathcal{L}\{f(t)\} \equiv \int_0^\infty e^{-pt} f(t) \mathrm{d}t \,. \tag{A.1}$$

The Laplace transform exists and is unique for all $p > a$ if $f(t)$ is piecewise continuous on every finite interval in $[0, \infty)$ and satisfies $|f(t)| \leq Me^{at}$ for all t in this domain. To find the inverse Laplace transform, one needs to evaluate the Bromwich contour integral

$$f(t) = \mathcal{L}^{-1}\{\bar{f}(p)\} \equiv \frac{1}{2\pi i} \int_{\gamma - i\infty}^{\gamma + i\infty} e^{pt} \bar{f}(p) \mathrm{d}p \,, \tag{A.2}$$

where γ is a vertical contour in the complex plane chosen such that all singularities of $\bar{f}(p)$ lie to the left of it. Often, however, we can find the relationship between $f(t)$ and its Laplace transform in tables, and table A.1 shows some examples for common functions. The Laplace transform is linear, so that for two functions $f(t)$, $g(t)$ and constants a, b, we have

$$\mathcal{L}\{af(t) + bg(t)\} = a\bar{f}(p) + b\bar{g}(p) \,. \tag{A.3}$$

The Laplace transform is particularly useful when considering differential equations, due to its unique behaviour when dealing with derivatives. Given that $f(t)$ is $n-1$ times continuously differentiable, we have

$$\mathcal{L}\{\partial_t^n f(t)\} = p^n \mathcal{L}\{f(t)\} - p^{n-1} f(0) - p^{n-2} \partial_t f(0) \ldots - \partial_t^{n-1} f(0) \,. \tag{A.4}$$

Furthermore, the Laplace transform of a convolution is the product of the Laplace transforms of each of the convoluted functions, in other words

$$\mathcal{L}\{f(t) * g(t)\} = \bar{f}(p)\bar{g}(p) \,, \tag{A.5}$$

where the convolution is defined as

$$f(t) * g(t) = \int_0^t f(\tau) g(t - \tau) \mathrm{d}\tau = g(t) * f(t) \,. \tag{A.6}$$

An important implication is

$$f(t) * g(t) = \mathcal{L}^{-1}\{\bar{f}(p)\bar{g}(p)\}\,. \tag{A.7}$$

Finally, for functions of several variables $f(x,t)$, the Laplace transform becomes

$$\bar{f}(x,p) = \int_0^\infty e^{-pt} f(x,t)\mathrm{d}t\,, \tag{A.8}$$

leading to the following useful relations:

$$\mathcal{L}\{\partial_x f(x,t)\} = \frac{\mathrm{d}\bar{f}(x,p)}{\mathrm{d}x} \tag{A.9}$$

$$\mathcal{L}\{\partial_x^2 f(x,t)\} = \frac{\mathrm{d}^2\bar{f}(x,p)}{\mathrm{d}x^2} \tag{A.10}$$

$$\mathcal{L}\{\partial_t f(x,t)\} = p\bar{f}(x,p) - f(x,0) \tag{A.11}$$

$$\mathcal{L}\{\partial_t^2 f(x,t)\} = p^2\bar{f}(x,p) - pf(x,0) - \partial_t f(x,0) \tag{A.12}$$

Table A.1: Laplace transforms and their inverses for some common functions. Note that a is a real constant.

$f(t)$	$\bar{f}(p)$
1	$\frac{1}{p}$
t	$\frac{1}{p^2}$
t^n	$\frac{1}{p^n}$
e^{at}	$\frac{1}{p-a}$
$\cos(at)$	$\frac{p}{p^2+a^2}$
$\sin(at)$	$\frac{a}{p^2+a^2}$
$\frac{a}{2\sqrt{\pi t^3}}\exp\left(-\frac{a^2}{4t}\right)$	$e^{-a\sqrt{p}}$

Appendix B

Model for dissolution of bulk nanobubble

Liquid velocity

The convective term in (2.11) is dependent on the velocity $\mathbf{v}_l = v_l(r,t)\,\hat{\mathbf{r}}$ of the liquid, in our case driven by the shrinking bubble. From mass conservation, it is clear that the velocity must be equal to[40]

$$v_l(r,t) = \frac{F(t)}{r^2}\,, \tag{B.1}$$

where $F(t)$ is some function which comes from the boundary condition at the interface. Since the liquid at the interface has the same velocity as the bubble interface, we have

$$v_l(\mathcal{R},t) = \frac{F(t)}{\mathcal{R}^2} = \dot{\mathcal{R}}\,,$$

which can be combined with (B.1) to give

$$v_l(r,t) = \frac{\mathcal{R}^2}{r^2}\dot{\mathcal{R}}\,. \tag{B.2}$$

Inserting (B.2) in the convective term in (2.11) yields

$$-\nabla\cdot(\mathbf{v}_l C_l) = -\nabla\cdot\hat{\mathbf{r}}\left(\frac{\mathcal{R}^2}{r^2}\dot{\mathcal{R}}C_l\right) = -\frac{1}{r^2}\frac{\partial}{\partial r}\left(\mathcal{R}^2\dot{\mathcal{R}}C_l\right) = -\frac{\mathcal{R}^2}{r^2}\dot{\mathcal{R}}\partial_r C_l\,. \tag{B.3}$$

Mass balance at the interface

The scalar transport equation given by (2.11) also holds in the gas phase, and can be written

$$\dot{C}_g - D_g\nabla\cdot\nabla C_l + \nabla\cdot(\mathbf{v}_g C_g) = 0\,. \tag{B.4}$$

Since the hydrogen concentration is uniform inside the bubble, we set $\nabla C_g = 0$. Using this, and the relation

$$\nabla\cdot(\mathbf{v}_g C_g) = C_g\nabla\cdot\mathbf{v}_g + \mathbf{v}_g\cdot\nabla C_g\,,$$

allows us to rewrite (B.4) as

$$\dot{C}_g + C_g \nabla \cdot \mathbf{v}_g = 0\,.$$

With $\mathbf{v}_g = v_g\,\hat{\mathbf{r}}$ we then have

$$\nabla \cdot \mathbf{v}_g = \frac{1}{r^2}\frac{\partial (r^2 v_g)}{\partial r} = -\frac{\dot{C}_g}{C_g} = -\frac{\partial_{\mathcal{R}} C_g}{C_g}\,\dot{\mathcal{R}}\,.$$

Integration from the bubble center to its surface gives

$$\mathcal{R}^2 v_g(\mathcal{R}, t) = -\frac{\partial_{\mathcal{R}} C_g}{C_g}\,\dot{\mathcal{R}} \int_0^{\mathcal{R}} r^2 \mathrm{d}r = -\frac{\mathcal{R}^3}{3}\frac{\partial_{\mathcal{R}} C_g}{C_g}\,.$$

The velocity of the gas at the interface is therefore

$$v_g(\mathcal{R}, t) = -\frac{\mathcal{R}}{3}\frac{\partial_{\mathcal{R}} C_g}{C_g}\,. \tag{B.5}$$

From (B.2) we have that the liquid velocity at the interface equals

$$v_l(\mathcal{R}, t) = \dot{\mathcal{R}}\,. \tag{B.6}$$

If we introduce the fluxes $J_i = D_i \partial_r C_i$ for the phases $i \in \{g, l\}$, where D_i is the diffusion coefficient for hydrogen in phase i, a local mass balance at the interface ($r = \mathcal{R}$) is

$$-(J_l - J_g) + (C_l v_l - C_g v_g) = (C_l - C_g)\dot{\mathcal{R}}\,. \tag{B.7}$$

Since C_g is uniform, the flux J_g is zero, and we write $J_l = J$, denoting the flux in the liquid by the same symbol as used previously. Using this, and inserting (B.5) and (B.6) in (B.7), allows us to write

$$-J + \left(C_l \dot{\mathcal{R}} + \frac{\mathcal{R}}{3} \partial_{\mathcal{R}} C_g \dot{\mathcal{R}} \right) = (C_l - C_g)\dot{\mathcal{R}}\,.$$

The appropriate boundary condition at the interface is thus

$$J = D_l \partial_r C_l = \frac{1}{RT}\left(p_0 + \frac{4\gamma}{3\mathcal{R}} \right) \dot{\mathcal{R}}\,. \tag{B.8}$$

Conservation of hydrogen

In order to evaluate whether our system is behaving as expected, we seek a boundary condition at $r_{\max}$ which ensures that the amount of hydrogen molecules $n = n_g + n_l$ in the system is conserved. If it is, we have

$$\dot{n} = \dot{n}_g + \dot{n}_l = 0 \qquad \Longrightarrow \qquad \dot{n}_l = -\dot{n}_g\,. \tag{B.9}$$

The amount of hydrogen molecules inside the nanobubble is simply the (uniform) gas concentration times the nanobubble volume, i.e.

$$n_g = C_g \cdot \frac{4\pi \mathcal{R}^3}{3} = \frac{4\pi}{3RT}\left(p_0 \mathcal{R}^3 + 2\gamma \mathcal{R}^2 \right)\,,$$

so that the rate of change with respect to time is

$$\dot{n}_g = \frac{4\pi\mathcal{R}^2}{RT}\left(p_0 + \frac{4\gamma}{3\mathcal{R}}\right)\dot{\mathcal{R}} = 4\pi\mathcal{R}^2 \cdot J(\mathcal{R},t)\,.$$

The amount of hydrogen molecules in the liquid phase must be found by integrating over our spacial domain Ω. We consider a domain bounded by some large radial value $r_{\max}$, so that this integral becomes

$$n_l = \int_\Omega C_l(r,t)\mathrm{d}V = 4\pi\int_{\mathcal{R}}^{r_{\max}} C_l(r,t)r^2\mathrm{d}r\,.$$

To find the temporal derivative of n_l, we note Leibniz' integral rule:

$$\frac{\mathrm{d}}{\mathrm{d}\theta}\left(\int_{a(\theta)}^{b(\theta)} f(x,\theta)\,\mathrm{d}x\right) = \int_{a(\theta)}^{b(\theta)} \partial_\theta f(x,\theta)\,\mathrm{d}x \,+\, f\big(b(\theta),\theta\big)\cdot b'(\theta) \,-\, f\big(a(\theta),\theta\big)\cdot a'(\theta)$$

Applying this gives the rate of change of hydrogen molecules in the liquid as

$$\begin{aligned}\dot{n}_l &= 4\pi\frac{\mathrm{d}}{\mathrm{d}t}\left(\int_{\mathcal{R}}^{r_{\max}} C_l(r,t)r^2\mathrm{d}r\right)\\ &= 4\pi\left(\int_{\mathcal{R}}^{r_{\max}} \dot{C}_l(r,t)r^2\mathrm{d}r + C_l(r_{\max},t)r_{\max}^2\dot{r}_{\max} - C_l(\mathcal{R},t)\mathcal{R}^2\dot{\mathcal{R}}\right)\,. \qquad \text{(B.10)}\end{aligned}$$

Since $r_{\max}$ is held at a fixed value, its temporal derivative is zero. In order to evaluate the integral in the first term of (B.10), we note that the scalar transport equation for the hydrogen concentration in the liquid is

$$\dot{C}_l = D_l\nabla\cdot\nabla C_l - \dot{\mathcal{R}}\frac{\mathcal{R}^2}{r^2}\partial_r C_l\,.$$

We therefore have

$$\begin{aligned}&4\pi\int_{\mathcal{R}}^{r_{\max}} \dot{C}_l(r,t)r^2\mathrm{d}r\\ &= D_l\int_\Omega \nabla\cdot\nabla C_l(r,t)\mathrm{d}V - 4\pi\mathcal{R}^2\dot{\mathcal{R}}\int_{\mathcal{R}}^{r_{\max}} \partial_r C_l\mathrm{d}r\\ &= D_l\int_{\partial\Omega} \nabla C_l(r,t)\cdot\hat{\mathbf{n}}\,\mathrm{d}S - 4\pi\mathcal{R}^2\dot{\mathcal{R}}\int_{C_l(\mathcal{R},t)}^{C_l(r_{\max},t)} \mathrm{d}C_l\\ &= 4\pi D_l\left(r_{\max}^2\partial_r C_l(r_{\max},t) - \mathcal{R}^2\partial_r C_l(\mathcal{R},t)\right) - 4\pi\mathcal{R}^2\dot{\mathcal{R}}\left(C_l(r_{\max},t) - C_l(\mathcal{R},t)\right)\,,\end{aligned}$$

where we have exploited the divergence of the Laplacian and the divergence theorem. The rate of change of hydrogen molecules in the liquid is then

$$\dot{n}_l = 4\pi\left(r_{\max}^2 J(r_{\max},t) - \mathcal{R}^2 J(\mathcal{R},t) - \mathcal{R}^2\dot{\mathcal{R}}C_l(r_{\max},t)\right)\,.$$

In order for the amount of hydrogen molecules in the system to be constant, (B.9) must be fulfilled, i.e.

$$J(r_{\max},t) = \frac{\mathcal{R}^2}{r_{\max}^2}\dot{\mathcal{R}}\,C_l(r_{\max},t)\,.$$

A suitable boundary condition at $r = r_{\max}$ which should ensure that the amount of H_2 molecules in the system is conserved is therefore the Robin condition

$$C_l - \left(\frac{r_{\max}}{\mathcal{R}}\right)^2 \frac{D}{\dot{\mathcal{R}}} \partial_r C_l = 0 \,. \tag{B.11}$$

Domain mapping

Since the bubble radius enters into the PDE (3.9) which determines the hydrogen concentration in the liquid, and the concentration enters into the ODE (3.11) for the radius, we need to perform iterations in both equations for each time step and couple the results. Before we discretize the equations, however, we need to address a difficulty with the PDE, namely the time-dependency of the spatial domain Ω. When the bubble has radius $\mathcal{R}(t)$, and we set $r_{\max}$ as the largest distance from the bubble center to be considered, the domain is

$$\Omega(t) = [\mathcal{R}(t), r_{\max}] \times [0, \pi) \times [0, 2\pi) \,.$$

We wish to use the same grid $\Omega(0)$ to represent $\Omega(t)$ at all times, so we need to introduce a transformation $\Phi : \Omega(0) \to \Omega(t)$. We denote spherical coordinates in our real (physical) domain by (r, θ, ϕ), where r is the radius and θ and ϕ are azimuthal and polar angles, respectively, while in the reference domain we use $(\tilde{r}, \theta, \phi)$. We want the transformation to behave so that $\mathcal{R}(t) < r < r_{\max}$ and $\mathcal{R}_0 < \tilde{r} < r_{\max}$, which means that the far end of the time-dependent domain is held fixed while the starting point is streched like a rubber band as the bubble radius shrinks. Figure 3.5 illustrates the radial stretching. It is clear that the domain is stretched by a factor

$$s(t) = \frac{r_{\max} - \mathcal{R}}{r_{\max} - \mathcal{R}_0} \,,$$

so that the relationship between the time-independent position $\tilde{r}$ and the actual position r is

$$r_{\max} - r = s(r_{\max} - \tilde{r}) = \frac{r_{\max} - \mathcal{R}}{r_{\max} - \mathcal{R}_0}(r_{\max} - \tilde{r}) \,.$$

A suitable transformation is therefore

$$\Phi(\tilde{r}, t) : \Omega(0) \to \Omega(t) : (\tilde{r}, \theta, \phi) \mapsto (r, \theta, \phi) \ ,$$

where

$$r = s\tilde{r} - (s-1) r_{\max} \tag{B.12}$$

The Jacobian of this transformation is

$$\mathcal{D}\Phi = \frac{\partial(r, \theta, \phi)}{\partial(\tilde{r}, \theta, \phi)} = \begin{pmatrix} \frac{\partial r}{\partial \tilde{r}} & \frac{\partial r}{\partial \theta} & \frac{\partial r}{\partial \phi} \\ \frac{\partial \theta}{\partial \tilde{r}} & \frac{\partial \theta}{\partial \theta} & \frac{\partial \theta}{\partial \phi} \\ \frac{\partial \phi}{\partial \tilde{r}} & \frac{\partial \phi}{\partial \theta} & \frac{\partial \phi}{\partial \phi} \end{pmatrix} = \begin{pmatrix} s & 0 & 0 \\ 0 & 1 & 0 \\ 0 & 0 & 1 \end{pmatrix} ,$$

while its time derivative is

$$\dot{\Phi} = \frac{\partial r}{\partial t}\,\hat{\tilde{\mathbf{r}}}\,,$$

where

$$\frac{\partial r}{\partial t} = \frac{r_{\max} - \tilde{r}}{r_{\max} - \mathcal{R}_0}\,\dot{\mathcal{R}}\,. \tag{B.13}$$

Since an arc length element ds in the real-time spherical coordinates (r, θ, ϕ) is given by

$$\mathrm{d}s^2 = \mathrm{d}r^2 + r^2\mathrm{d}\theta^2 + r^2\sin^2\theta\mathrm{d}\phi^2\,,$$

the covariant metric tensor is

$$g(r,\theta,\phi) = \begin{pmatrix} 1 & 0 & 0 \\ 0 & r^2 & 0 \\ 0 & 0 & r^2\sin^2\theta \end{pmatrix}.$$

The covariant metric tensor in terms of the reference coordinates $(\tilde{r}, \theta, \phi)$ is then

$$g(\tilde{r},\theta,\phi) \equiv g = \mathcal{D}\Phi^T g(r,\theta,\phi)\mathcal{D}\Phi = \begin{pmatrix} s^2 & 0 & 0 \\ 0 & r^2 & 0 \\ 0 & 0 & r^2\sin^2\theta \end{pmatrix}, \tag{B.14}$$

with determinant

$$\det(g) = s^2 r^4 \sin^2\theta\,.$$

Transformation of PDE

The hydrogen concentration in the liquid in our reference domain is denoted $\tilde{C}_l$, and with the transformed nabla operator denoted $\tilde{\nabla}$, we get the following transformation relations.

$$C_l\left(r,t\right) = C_l\left(\Phi(\tilde{r},t),t\right) = \tilde{C}_l(\tilde{r},t)$$

$$\nabla C_l\left(r,t\right) = \nabla C_l\left(\Phi(\tilde{r},t),t\right) = \mathcal{D}\Phi^{-T}\tilde{\nabla}\tilde{C}_l(\tilde{r},t)$$

$$\dot{C}_l\left(r,t\right) = \dot{\tilde{C}}_l(\Phi(r,t),t) - \nabla C_l\left(\Phi(\tilde{r},t),t\right)\dot{\Phi}(\tilde{r},t) = \dot{\tilde{C}}_l(\tilde{r},t) - \mathcal{D}\Phi^{-T}\tilde{\nabla}\tilde{C}_l(\tilde{r},t)\dot{\Phi}(\tilde{r},t)$$

$$\Delta C_l\left(r,t\right) = \Delta C_l\left(\Phi(\tilde{r},t),t\right) = \frac{1}{\sqrt{\det(g)}}\tilde{\nabla}\cdot\left(\sqrt{\det(g)}g^{-1}\tilde{\nabla}\tilde{C}_l(\tilde{r},t)\right)$$

These identities allow us to rewrite the PDE (3.9) in the transformed coordinate system.

$$
\begin{aligned}
\dot{\tilde{C}}_l - \mathcal{D}\Phi^{-T}\tilde{\nabla}\tilde{C}_l\,\dot{\Phi} - \frac{D_l}{\sqrt{\det(g)}}\tilde{\nabla}\cdot\left(\sqrt{\det(g)}g^{-1}\tilde{\nabla}\tilde{C}_l\right)& \\
+\frac{\mathcal{R}^2\dot{\mathcal{R}}}{r^2}\mathcal{D}\Phi^{-T}\tilde{\nabla}\tilde{C}_l\cdot\hat{\tilde{\mathbf{r}}} &= 0 \qquad \text{on} \quad \tilde{r} > \mathcal{R}_0 \\
\tilde{C}_l - \left(\frac{r_{\max}}{\mathcal{R}}\right)^2\frac{D_l}{\dot{\mathcal{R}}}\mathcal{D}\Phi^{-T}\tilde{\nabla}\tilde{C}_l\cdot\hat{\tilde{\mathbf{r}}} &= 0 \qquad \text{at} \quad \tilde{r} = r_{\max} \\
\tilde{C}_l - \frac{D_l}{\alpha}\mathcal{D}\Phi^{-T}\tilde{\nabla}\tilde{C}_l\cdot\hat{\tilde{\mathbf{r}}} &= HC_g \qquad \text{at} \quad \tilde{r} = \mathcal{R}_0 \\
\tilde{C}_l(\tilde{r},0) &= 0 \qquad \text{on} \quad \tilde{r} > \mathcal{R}_0
\end{aligned}
$$

To simplify, we note the following relations.

$$
\begin{aligned}
\mathcal{D}\Phi^{-T}\tilde{\nabla}\tilde{C}_l &= \frac{1}{s}\,\partial_{\tilde{r}}\tilde{C}_l\,\hat{\tilde{\mathbf{r}}} \\
\mathcal{D}\Phi^{-T}\tilde{\nabla}\tilde{C}_l\,\dot{\Phi} &= \frac{1}{s}\,\frac{r_{\max}-\tilde{r}}{r_{\max}-\mathcal{R}_0}\,\dot{\mathcal{R}}\,\partial_{\tilde{r}}\tilde{C}_l\,, \\
\sqrt{\det(g)} &= sr^2\sin\theta\,, \\
g^{-1}\cdot\tilde{\nabla}\tilde{C}_l &= \frac{1}{s^2}\,\partial_{\tilde{r}}\tilde{C}_l\,\hat{\tilde{\mathbf{r}}}\,,
\end{aligned}
$$

$$
\begin{aligned}
\Delta C_l &= \frac{1}{\sqrt{\det(g)}}\tilde{\nabla}\cdot\left(\sqrt{\det(g)}g^{-1}\tilde{\nabla}\tilde{C}_l\right) = \frac{1}{sr^2\sin\theta}\tilde{\nabla}\cdot\left(\frac{r^2\sin\theta}{s}\partial_{\tilde{r}}\tilde{C}_l\,\hat{\tilde{\mathbf{r}}}\right) \\
&= \frac{1}{s^2r^2}\frac{\partial}{\partial\tilde{r}}\left(r^2\partial_{\tilde{r}}\tilde{C}_l\right) = \frac{1}{s^2r^2}\left(2r\frac{\partial r}{\partial\tilde{r}}\partial_{\tilde{r}}\tilde{C}_l + r^2\partial^2_{\tilde{r}}\tilde{C}_l\right) = \frac{1}{s^2}\left(\frac{2s}{r}\,\partial_{\tilde{r}}\tilde{C}_l + \partial^2_{\tilde{r}}\tilde{C}_l\right) \\
&= \frac{1}{s^2}\left(\frac{2s}{s\tilde{r}-(s-1)r_{\max}}\,\partial_{\tilde{r}}\tilde{C}_l + \partial^2_{\tilde{r}}\tilde{C}_l\right)
\end{aligned}
$$

By using these relations, our PDE becomes:

$$
\begin{aligned}
\dot{\tilde{C}}_l + \frac{1}{s}\left(\left(\frac{\mathcal{R}}{s\tilde{r}-(s-1)r_{\max}}\right)^2 - \frac{r_{\max}-\tilde{r}}{r_{\max}-\mathcal{R}_0}\right)\dot{\mathcal{R}}\,\partial_{\tilde{r}}\tilde{C}_l& \\
-\frac{D_l}{s^2}\left(\frac{2s}{s\tilde{r}-(s-1)r_{\max}}\,\partial_{\tilde{r}}\tilde{C}_l + \partial^2_{\tilde{r}}\tilde{C}_l\right) &= 0 \qquad \text{on } \tilde{r} > \mathcal{R}_0 \\
\tilde{C}_l - \frac{1}{s}\left(\frac{r_{\max}}{\mathcal{R}}\right)^2\frac{D_l}{\dot{\mathcal{R}}}\,\partial_{\tilde{r}}\tilde{C}_l &= 0 \qquad \text{at } \tilde{r} = r_{\max} \\
\tilde{C}_l - \frac{1}{s}\,\frac{D_l}{\alpha}\,\partial_{\tilde{r}}\tilde{C}_l &= HC_g \qquad \text{at } \tilde{r} = \mathcal{R}_0 \\
\tilde{C}_l(\tilde{r},0) &= 0 \qquad \text{on } \tilde{r} > \mathcal{R}_0
\end{aligned}
$$

Appendix C

Numerical methods

The finite-element method

Strong formulation of problem statement

We wish to find a solution $u(x, y, z)$ with integrable first-derivatives on the domain $\Omega \in \mathbb{R}^3$ such that

$$\Delta u = -f(x, y, z) \qquad \text{in } \Omega\,, \tag{C.1a}$$

$$u = g_D(x, y, z) \qquad \text{on } \partial\Omega_D\,, \tag{C.1b}$$

$$\frac{\partial u}{\partial n} = g_N(x, y, z) \qquad \text{on } \partial\Omega_N\,, \tag{C.1c}$$

$$au + b\frac{\partial u}{\partial n} = g_R(x, y, z) \qquad \text{on } \partial\Omega_R\,, \tag{C.1d}$$

where the functions f, g_D, g_N and g_R and the constants a and b are known. Here, $\partial/\partial n$ represents the normal derivative on a surface, while $\partial\Omega_D$, $\partial\Omega_N$ and $\partial\Omega_R$ represent the parts of the boundary surface $\partial\Omega$ where Dirichlet, Neumann and Robin boundary conditions are implemented, respectively.

Weak formulation

To obtain a variational formulation of our problem, we multiply (C.1a) by a test function $v(x, y, z)$ and integrate by parts over Ω.

$$\begin{aligned}\int_\Omega fv\,\mathrm{d}V &= -\int_\Omega v\nabla^2 u\,\mathrm{d}V = -\left(\int_{\partial\Omega} v\nabla u\cdot \mathrm{d}\mathbf{S} - \int_\Omega \nabla u\cdot\nabla v\,\mathrm{d}V\right)\\ &= -\int_{\partial\Omega_N} g_N v\,\mathrm{d}S - \frac{1}{b}\int_{\partial\Omega_R} g_R v\,\mathrm{d}S + \frac{a}{b}\int_{\partial\Omega_R} uv\,\mathrm{d}S + \int_\Omega \nabla u\cdot\nabla v\,\mathrm{d}V \end{aligned} \tag{C.2}$$

The surface integral over the Dirichlet boundary vanishes since we demand $v|_{\partial\Omega_D} = 0$. Rewriting (C.2) gives us a weak formulation of our problem: Find $u \in H^1(\Omega)$ such that

$$a(u, v) = l(v) \qquad \forall v \in H^1_{\partial\Omega_D}\,, \tag{C.3}$$

where the bilinear form $a(\,\cdot\,,\,\cdot\,)$, linear functional $l(\,\cdot\,)$ and function space $H^1_{\partial\Omega_D}$ are

$$a(u, v) = \int_\Omega \nabla u \cdot \nabla v \,\mathrm{d}V + \frac{a}{b}\int_{\partial\Omega_R} uv \,\mathrm{d}S\,, \tag{C.4}$$

$$l(v) = \int_\Omega fv \,\mathrm{d}V + \int_{\partial\Omega_N} g_N v \,\mathrm{d}S + \frac{1}{b}\int_{\partial\Omega_R} g_R v \,\mathrm{d}S \tag{C.5}$$

$$H^1_{\partial\Omega_D} = \{v \in H^1(\Omega) : v|_{\partial\Omega_D} = 0\}\,. \tag{C.6}$$

We still need to do some manipulation, since we currently seek u and v in different function spaces. To fix this, we introduce a lifting function $R_g(x, y, z) \in H^1(\Omega)$ which has the same value as u on the Dirichlet boundary, $R_g|_{\partial\Omega_D} = g_D$. We then seek a lifted solution $\mathring{u} = u - R_g$ which is in the same space as v. Noting that $\nabla u = \nabla\mathring{u} + \nabla R_g$, our final weak formulation becomes: Find $\mathring{u} \in H^1_{\partial\Omega_D}(\Omega)$ such that

$$a(\mathring{u}, v) = F(v) \qquad \forall v \in H^1_{\partial\Omega_D}\,, \tag{C.7}$$

where our new linear functional $F(\,\cdot\,)$ is given by

$$F(v) = \int_\Omega fv \,\mathrm{d}V + \int_{\partial\Omega_N} g_N v \,\mathrm{d}S + \frac{1}{b}\int_{\partial\Omega_R} g_R v \,\mathrm{d}S - \int_\Omega \nabla R_g \cdot \nabla v \,\mathrm{d}V - \frac{a}{b}\int_{\partial\Omega_R} R_g v \,\mathrm{d}S\,. \tag{C.8}$$

The solution to the weak problem is then $u = \mathring{u} + R_g$.

Galerkin projection

To solve our system numerically, we need to discretize the problem. We look for a solution u_h in a subspace $X_h \subset H^1_{\partial\Omega_D}$ and let Ω be discretized into M tetrahedra K_k. The space X_h is the subset of functions in $H^1_{\partial\Omega_D}$ that are linear on each element, i.e.

$$X_h = \{v \in H^1_{\partial\Omega_D} : v|_{K_k} \in \mathbb{P}_1(K_k), 1 \le k \le M\}\,. \tag{C.9}$$

We construct one basis function ϕ_i for each of the N nodes p_i in our mesh, such that

$$X_h = \operatorname{span}\{\phi_i\}_{i=1}^N$$

and

$$\phi_j(p_i) = \delta_{ij} = \begin{cases} 1\,, & i = j \\ 0\,, & i \neq j \end{cases}$$

where δ_{ij} is the Kronecker delta. When we search for a solution $u_h \in X_h$ we can write this as $u_h = \sum_{i=1}^N u_h^i \phi_i$. We insert this into the weak formulation (C.7) and use that $a(\,\cdot\,,\,\cdot\,)$ is bilinear to take the sum and coefficients outside. Since ϕ_i is a basis for X_h , it is sufficient to require that the weak formulation holds for all the basis functions

$$\sum_{i=1}^{N} u_h^i a(\phi_i, \phi_j) = l(\phi_j)\,, \quad j = 1, 2, ..., N\,.$$

This set of equations can be written as

$$\mathbf{A} \cdot \mathbf{u} = \mathbf{b}\,, \tag{C.10}$$

where the stiffness matrix **A**, displacement vector **u** and load vector **b** are given by

$$\mathbf{A} = [A_{ij}] = [a(\phi_i, \phi_j)]\,, \tag{C.11}$$

$$\mathbf{u} = [u_h^i] \tag{C.12}$$

$$\mathbf{b} = [f_i] = [l(\phi_i)]\,, \tag{C.13}$$

respectively. (C.10) can be solved numerically as long as we have a numerical integration procedure to calculate the integrands in (C.4) and (C.8).

Numerical integration

There are several methods for integrating functions over a given domain numerically. One of the most popular schemes for evaluating integrals in 2 and 3 dimensions is n-point Gaussian quadrature, in which the approximation is done by weighted summation of function values at n different points in the domain. To be able to use this method, we need to have an explicitly defined function $f(x)$. In one dimension, the scheme can be written as

$$\int_{-1}^{1} f(x)\mathrm{d}x \approx \sum_{i=1}^{n} w_i f(x_i)\,, \tag{C.14}$$

where f is the function to be approximated and w_i are the weights at the points x_i. Since we are often interested in domains other than $-1 \leq x \leq 1$, we can shift the integrand in (C.14) to get the approximation on an arbitrary interval $a \leq x \leq b$.

$$\int_{a}^{b} f(x)\,\mathrm{d}x = \frac{b-a}{2} \int_{-1}^{1} f\left(\frac{b-a}{2} z + \frac{a+b}{2}\right) \mathrm{d}z. \tag{C.15}$$

The quadrature can be extended to d dimensions as

$$\int_{\Omega} f(\mathbf{x})\mathrm{d}\mathbf{x} \approx \sum_{i=1}^{n} w_i f(\mathbf{x_i})\,, \tag{C.16}$$

where the point vectors $\mathbf{x_i}$ have d components. The domain Ω is made up of triangles in 2D and tetrahedra in 3D, with $d+1$ corner points $\mathbf{p}_j$. We map to barycentric coordinates $\boldsymbol{\zeta}$ as our reference domain, given by

$$\mathbf{x} = \sum_{j=1}^{d+1} \zeta_j \mathbf{p}_j\,. \tag{C.17}$$

The weights w_i used for Gaussian quadrature in two and three dimensions are listed in tables C.1 and C.2, respectively.

Table C.1: Barycentric coordinates and weights for n-point Gaussian quadrature in 2D for 1, 3 and 4 points.

n	ζ_1	ζ_2	ζ_3	w
1	1/3	1/3	1/3	1
3	1/2	1/2	0	1/3
	1/2	0	1/2	1/3
	0	1/2	1/2	1/3
4	1/3	1/3	1/3	-9/16
	3/5	1/5	1/5	25/48
	1/5	3/5	1/5	25/48
	1/5	1/5	3/5	25/48

Table C.2: Barycentric coordinates and weights for n-point Gaussian quadrature in 3D for 1, 4 and 5 points.

n	ζ_1	ζ_2	ζ_3	ζ_4	w
1	1/4	1/4	1/4	1/4	1
4	$\frac{5+3\sqrt{5}}{20}$	$\frac{5-\sqrt{5}}{20}$	$\frac{5-\sqrt{5}}{20}$	$\frac{5-\sqrt{5}}{20}$	1/4
	$\frac{5-\sqrt{5}}{20}$	$\frac{5+3\sqrt{5}}{20}$	$\frac{5-\sqrt{5}}{20}$	$\frac{5-\sqrt{5}}{20}$	1/4
	$\frac{5-\sqrt{5}}{20}$	$\frac{5-\sqrt{5}}{20}$	$\frac{5+3\sqrt{5}}{20}$	$\frac{5-\sqrt{5}}{20}$	1/4
	$\frac{5-\sqrt{5}}{20}$	$\frac{5-\sqrt{5}}{20}$	$\frac{5-\sqrt{5}}{20}$	$\frac{5+3\sqrt{5}}{20}$	1/4
5	1/4	1/4	1/4	1/4	-4/5
	1/2	1/6	1/6	1/6	9/20
	1/6	1/2	1/6	1/6	9/20
	1/6	1/6	1/2	1/6	9/20
	1/6	1/6	1/6	1/6	9/20

For cases when the function value is known only at specific points $\{\mathbf{x}_i\}$, we cannot generally use Gaussian quadrature. We therefore introduce a simple Newton-Cotes quadrature called the trapezoidal rule, given by

$$\int_a^b f(x)\mathrm{d}x \approx \frac{f(a)+f(b)}{2}\,(b-a)\,. \tag{C.18}$$

For a closed interval $[a, b]$, which is discretized by the points $x_0, x_1, \ldots, x_N$ where the function values are known, the trapezoidal rule can be applied on each subinterval to yield

$$\int_a^b f(x)\mathrm{d}x = \sum_{i=0}^{N-1} \int_{x_i}^{x_{i+1}} f(x)\mathrm{d}x \approx \frac{1}{2} \sum_{i=0}^{N-1} (x_{i+1} - x_i) \left(f(x_i) + f(x_{i+1}) \right) . \tag{C.19}$$

The finite-difference method

Taylor's formula

Let $f \in C^{n+1}(I)$ where $I \subset \mathbb{R}$ is an interval on the real line, i.e. f is $n+1$ times continuously differentiable on I. Then the following formula holds if $x \in I$ and $x + h \in I$:

$$f(x+h) = \sum_{m=0}^{n} \frac{h^m}{m!} \partial_x^m f(x) + \mathcal{O}(h^{n+1}) \tag{C.20}$$

The Big-$\mathcal{O}$ notation means that the remainder outside the sum is of order h^{n+1}, and thus becomes insignificant when h is set to a small value. Taylor's formula is the foundation on which the method of finite differences is built.

Domain discretization and truncation error

To approximate the derivatives of the function f by finite differences, we first introduce a grid of equidistant points x_n such that $x_{n+1} = x_n + h$, and define

$$f_n = f(x_n) \quad \text{and} \quad f_n^{(m)} = \partial_x^m f(x_n) \, . \tag{C.21}$$

Our goal is approximate the derivatives $f_n^{(m)}$ at the gridpoints with expressions of the type $\sum_{l=p}^{q} a_l f_{n+l}$, where q and p are integers. To get the best possible approximation for $f_n^{(m)}$, we therefore introduce the truncation error

$$\tau_n(h) = \sum_{l=p}^{q} a_l f_{n+l} - f_n^{(m)} \, , \tag{C.22}$$

which we seek to minimize.

Method of undetermined coefficients

In the method of undetermined coefficients, we choose which neighbouring points to approximate by (p and q) and which derivative we want to approximate (m). From (C.20) and (C.21) we have

$$f_{n+l} = f(x_n + lh) = \sum_{k=0}^{\nu} \frac{(lh)^k}{k!} f_n^{(k)}(x) + \mathcal{O}(h^{\nu+1}) \tag{C.23}$$

where $\nu \geq m$. The truncation error is then given by

$$\tau_n = \sum_{k=0}^{\nu} \frac{h^k}{k!} \left(\sum_{l=p}^{q} a_l l^k \right) u_n^{(k)} - u_n^{(m)} + \mathcal{O}(h^{\nu+1}) \, , \tag{C.24}$$

and we want to achieve $\tau_n = \mathcal{O}(h^r)$ for the largest possible value of r. The method of undetermined coefficients is then to choose the coefficients $a_p, \ldots, a_q$ such that

$$\frac{h^k}{k!}\sum_{l=p}^{q} a_l l^k = \begin{cases} 0\,, & 0 \leq k \leq m-1 \\ 1\,, & k = m \\ 0\,, & m+1 \leq k \leq j \end{cases} \tag{C.25}$$

where $j = q - p \geq m$. Some useful difference formulae we have used are listed in table C.3.

Table C.3: Some finite-difference formulae for first and second order derivatives.

m	p	q	$f_n^{(m)}$	Truncation error
1	-1	1	$\frac{1}{2h}(f_{n+1} - f_{n-1})$	$\mathcal{O}(h^2)$
1	0	1	$\frac{1}{h}(f_{n+1} - f_n)$	$\mathcal{O}(h)$
1	0	2	$\frac{1}{2h}(-3f_n + 4f_{n+1} - f_{n+2})$	$\mathcal{O}(h^2)$
1	-2	0	$\frac{1}{2h}(3f_n - 4f_{n-1} + f_{n-2})$	$\mathcal{O}(h^2)$
2	-1	1	$\frac{1}{h^2}(f_{n+1} - 2f_n + f_{n-1})$	$\mathcal{O}(h^2)$